Synthesis and Characterization of MnFe$_2$O$_4$@ZnO-GO and MnFe$_2$O$_4$@ZnO-rGO Nanocomposites with Evaluation of Improved Photocatalytic Performance under Sun Light

Azam Zamani [1], Alireza Mahjoub [2*], Mirabdullah Seyed Sadjadi [1]

[1] *Department of Chemistry, Science and Research Branch, Islamic Azad University, Tehran, Iran*

[2] *Department of Chemistry, Tarbiat Modares University, Tehran, Iran*

ARTICLE INFO

ABSTRACT

A facile hydrothermal synthesis route was used to synthesize MnFe$_2$O$_4$@ZnO–GO and MnFe$_2$O$_4$@ZnO–rGO nanocomposites at low temperature of 180 °C for 3h. We reported the successful synthesis of the MnFe$_2$O$_4$@ZnO nanocomposite via the co-precipitation method and was calcined at 200 °C for 3 h. Our synthesis of MnFe$_2$O$_4$@ZnO modified by the different weight percentages of GO and RGO. The as-synthesized samples were investigated by techniques XRD, FE-SEM, EDX, TEM, FT-IR, UV-DRS, PL, BET. TEM observations have displayed that MnFe$_2$O$_4$@ZnO nanoparticles were deposited on the graphene oxide and reduced graphene oxide surface. Magnetic studies demonstrated that the MnFe$_2$O$_4$@ZnO–GO and MnFe$_2$O$_4$@ZnO–rGO nanocomposites can be used as a magnetically separable photocatalyst. The photodegradation efficiency of the prepared materials was evaluated by the decomposition of Congo Red (CR) in 35 min of natural sunlight irradiation. Among the synthesized materials, the MnFe$_2$O$_4$@ZnO-GO photocatalyst showed maximum photocatalytic activity (99.54 %). The effect of examining different photocatalytic parameters demonstrated that, the photocatalytic activity of MnFe$_2$O$_4$@ZnO-GO and MnFe$_2$O$_4$@ZnO-rGO composite increases with decreasing CR dye concentration, increasing the photocatalyst dosage and in acidic pH. We also investigated the role of some scavengers in the degradation procedures to study the effect of active species. The studies from the radical scavengertests showed that active radicals like $^{\bullet}$O$_2$$^{-}$, e, h^{+}, and $^{\bullet}$OH were involved in the photodegradation of CR dye. The experimental results were applied to illustrate the proposed mechanism ability for improved photocatalysis. The Kinetics investigations have revealed that the degradation of CR by the prepared photocatalysts follows the pseudo-first-order kinetics and the rate constant attained for MnFe$_2$O$_4$@ZnO-GO (k = 78.10^{-3} min^{-1}) was higher than of MnFe$_2$O$_4$@ZnO-rGO (k = 57.10^{-3} min^{-1}).

* Corresponding Author Email: mahjouba@modares.ac.ir

INTRODUCTION

In recent decades, environmental pollution and its related effects have investigated considerable problems that increasingly confront human societies [1]. Because of the variety of manufactured products, the wastewater, including pollutants has converted into a worldwide public health subject [2–4]. Textile industries are the most distinctive sections in the world which uses dye to color the fabrics. The presence of organic pollutants in water is a serious threat to the public health for human and wildlife because of their high toxicity [5-7]. Thus, people are increasingly upset about the dyeing wastewater treatment, which is highly colored and toxic to the environment. Colored water affects the visibility of water and prevents sunlight influence to the stream [8]. Among dyes, CR is extensively employed in textile industries. Congo red cannot be effectively decolorized mainly because of they are developed to resist fading, leading to biological degradation. The difficulties related to dyeing wastewater treatment have motivated people to develop advanced water purification approach. A large body of research has been performed in developing dye removal in water. Nano-semiconductor photocatalysts offer a very suitable way for removing the different organic pollutants which can be easily degraded under UV or solar light irradiation in the presence of photocatalysts [9-10]. It is well known that it is hard to separate and recover the nano-sized photocatalysts from the solutions by a simple method. Therefore, the nano-semiconductors in water would lead to a second contamination. Magnetic separation is an efficient attack to recover the magnetic particles by an applied magnetic field. Recently, magnetic photocatalysts composed of magnetic particles and photocatalysts have attracted very interest [11-12]. Magnetic nanoparticles (MNPs) have enticed a tremendous attention for their potential use in biomedical applications like controlled drug delivery, cell separation, magnetic resonance imaging and localized hyperthermia therapy of cancer. Iron oxide based magnetic nanoparticles are of particular importance due to their appropriate biocompatibility and low toxicity [13]. Among Magnetic nanoparticles, Spinel ferrites as MnFe$_2$O$_4$are chemically and thermally stable magnetic nanoparticles with small band gaps About 2 eV which leading to high photocatalytic activity under visible light irradiation [14-15]. Also, Zinc oxide (ZnO) is a semiconductor with a wide band gap width (3.37 eV) and large excitation binding energy (60 meV) at room temperature, which lead to ZnO has been used extensively in the degradation of dye pollutant [16]. The main difficulty of pure semiconductor photocatalysts is that the photo generated electron–hole pairs have faster recombination rates,which lead to reduce the photodegradation efficiency of the semiconductor activity photocatalysts [17-18]. Carbonaceous nanomaterials have been used for modifying semiconductor photocatalysts for efficiently transporting electrons [19]. Graphene oxide (GO) is one of the most good predecessor of graphene and has attracted great attention for its unique physicochemical properties. So, Graphene, an atomic sheet of sp^2 bonded carbon atoms, has been known as an ideal candidate for a variety of applications because of its high surface area, good electrical conductivity, mechanical and thermal properties, while the surface of GO is decorated with various hydrophilic oxygen containing functional groups. Inorganic materials modified with partially GO have been reported to show enhanced photocatalytic properties [20]. A few research studies have reported on metal oxide nanocomposites and nanocomposites with graphene and graphene derivatives; although, these reported composites endure from low-efficiency photocatalysis. There are few researches such as (Nd-ZrO2–GO) nanocomposite reports the degradation of only 20 ppm eosin Y dye in 180 min [21], composite of GO–ZrO$_2$ decomposes rhodamine B 30 ppm in 105 min[22], and some studies report on the removal of inorganic metals such as As(III), As(V) and Cr(VI) ion [23], but only synthesize MnFe$_2$O$_4$@ZnO on graphene oxide and reduced graphene oxide nanosheets has not yet been reported for the photocatalytic degradation of Congo red in 35 min of natural sunlight irradiation. As far as we know, our work is the first attempt to synthesize (MnFe$_2$O$_4$@ZnO/RGO) and (MnFe$_2$O$_4$@ZnO/GO) Composites using a facile hydrothermal route at low temperature of 180 °C for 3h. A facile co-precipitation approach was used for synthesizing MnFe$_2$O$_4$@ZnO nanocomposites and the as-synthesized materials were calcined at 200 °C for 3 h. Additionally, this co-precipitation method could be ascribed to the larger surface area, unique morphology, better homogeneity and

non-agglomerated of the synthesized particles. The photocatalytic activity of the as-prepared MnFe$_2$O$_4$@ZnO-graphene oxide and MnFe$_2$O$_4$@ZnO-reduced graphene oxide nanocomposites were investigated using Congo red as a model pollutant in 35 min of natural sunlight irradiation. Our synthesis of MnFe$_2$O$_4$@ZnO nanocomposites modified by the different weight percentages of GO and rGO as a visible-light photocatalyst might help to acquire Magnetically Separable photocatalysts for controlling environmental contaminants.

MATERIALS AND METHODS
Materials

All the chemicals that were employed in the experiments were reagent grade such as graphite powder (Merck, Germany 99.99% purity), 98% H$_2$SO$_4$ (Merck, Germany), KMnO$_4$ (Merck, Germany), 30% H$_2$O$_2$ (Merck, Germany), HCl (Merck, Germany), NH$_4$OH (Merck, Germany), Mn (NO$_3$)$_2$.4H$_2$O (Merck, Germany), Zn (NO$_3$)$_2$.4H$_2$O (Merck, Germany) and Fe (NO$_3$)$_2$·9H$_2$O (Merck, Germany). All the experiments were performed in aqueous media.

Instrumentation

The crystalline structure of MnFe$_2$O$_4$@ZnO/GO and MnFe$_2$O$_4$@ZnO/RGO were characterized by XRD (Philips PW 1730 Japan model) with CuK$_\alpha$ radiation (1.5406) ˚A in2θ scan range of 10–80°. In order to examine the morphologies of MnFe$_2$O$_4$@ZnO/GO and MnFe$_2$O$_4$@ZnO/RGO nanoparticles, TEM measurements were performed on a Zeiss-EM10C-100KV TEM instrument (Germany) and FESEM measurements were done with a ZEISS DSM-960A analytic microscope (Germany). Then, A diffuse reflectance spectrum (DRS) of the MnFe$_2$O$_4$@ZnO/GO and MnFe$_2$O$_4$@ZnO/RGO nanocomposites were recorded on a UV-2550 Shimadzu UV–vis spectrophotometer equipped with ISR-2200 DRS accessory (UV-2550 Shimadzu, Japan). PL emission spectra of the samples were analyzed at room temperature using a JASCO Spectrofluorometer (FP-8200). The specific surface area, pore distribution and pore parameters were studied by Brunauer–Emmet–Teller nitrogen adsorption–desorption isotherm at 77 k using Belsorp mini II instrument .Finally, IR spectra were recorded on a Bruker FT-IR instrument using KBr plates.

Synthesis of the MnFe$_2$O$_4$@ZnO nanoparticles

MnFe$_2$O$_4$@ZnO nanoparticles were carried out by facile co-precipitation method . Firstly, two transparent solutions were achieved when 4.75 g of Mn (NO$_3$)$_2$.4H$_2$O and 5.87 g of Fe (NO$_3$)$_2$·9H$_2$O dissolved in 40 ml of distilled water were mixed under magnetic stirring for 10 min at ambience temperature. Then, 25% NH$_4$OH was added dropwise into solution and a dark brown suspension was obtained. The Mn–Fe precursor was kept under magnetic stirring for 15 min. In addition, 1 g of Zn (NO$_3$)$_2$.4H$_2$O dissolved in 30 ml of distilled water were mixed under magnetic stirring for 10 min. After the Mn–Fe precursor solution was added to the suspension, the new mixture was stirred for 30 min in the dark at 90 °C for 2 h. In the following stage, the obtained residue was filtered and washed with ultrapure water for various times and dried at 70 °C overnight. Finally, the residue was calcined at 200 °C for 3 h to form MnFe$_2$O$_4$@ZnO nanoparticles.

Synthesis of graphene oxide

Modified Hummer's Method was employed using natural graphite flakes for the synthesis of GO [24]. In a typical synthesis, 9 g graphite flake was added in 25 ml of sulfuric acid (98%) and the mixture was sonicated to produce a fine dispersion. Then, This suspension was heated for 6 hours at 80 °C under magnetic stirring. 30g of potassium permanganate was added slowly to the mixture during the stirring process. The mixture was cooled to below 10 °C. Further, The mixture was stirred under ice water bath for two hours. And so, This solution was diluted with distilled water and treated with20 ml of hydrogen peroxide (30%) and was kept undisturbed for 24 hours for precipitation. The resulting GO solution was centrifuged and was washed several times with hydrochloric acid and distilled water and then, the precipitate was dried in a vacuum oven at 60 °C for 12 h.

Synthesis of reduced graphene oxide

To obtain reduced graphene oxide, hydrazine hydrate was employed as the reducing agent. The as prepared GO was dispersed into 200 ml water under mild ultrasound yielding a yellow-brown suspension. And so, 4 ml hydrazine hydrate (80wt. %) was added drop-wise and the solution was heated in a water bath for 24 h at 80 °C. In the next

stage, the prepared rGO product was washed with distilled water and collected by vacuum filtration.

Synthesis of the MnFe$_2$O$_4$@ZnO/GO nanoparticles

The MnFe$_2$O$_4$@ZnO-graphene oxide nanocomposites were synthesized using the hydrothermal method [25]. 1000 mg of GO was dispersed in 50 ml of distilled water with sonication at ambience temperature for 1 h. Then, 200 mg MnFe$_2$O$_4$@ZnO suspension was added and the mixture stirred for 30 min at room temperature to produce a MnFe$_2$O$_4$@ZnO-GO dispersion. The reaction resulting was transferred to a 100 ml Teflon-lined stainless steel autoclave , put in a 180 °C oven for 3hours in static conditions, and then cooled. After washing the residue with distilled water(two times), it was centrifuged and isolated. and Then, dried in a vacuum oven at 60 °C for 12 h. Three *MnFe$_2$O$_4$@ZnO/GO* nanocomposites with 0.1, 0.05, and 0.02 g *GO* were prepared.

Synthesis of the MnFe$_2$O$_4$@ZnO/rGO nanoparticles

The hydrothermal method was used to synthesize the MnFe2O4@ZnO-reduced graphene oxide nanocomposites [25]. 1000 mg of rGO was dispersed in 50 ml of ultrapure water with ultrasonication at ambience temperature for 1 h to form a stable rGO suspension. And so, 200 mg MnFe$_2$O$_4$@ZnO suspension was added and the solution stirred for 30 min at room temperature to produce a MnFe$_2$O$_4$@ZnO-rGO dispersion. The reaction resulting was transferred to a 100 ml Teflon-lined stainless steel autoclave and heated to 180 °C for 3 h. The reaction mixture was allowed to cool to room temperature. The acquired solution was centrifuged at 2000 rpm for 4 minutes. the residue was filtered, washed with ultrapure water(two times) and ethanol(one time). Then, residues were dried in a vacuum oven at 60 °C for 12 h. Three *MnFe$_2$O$_4$@ZnO/rGO* nanocomposites with 0.1, 0.05, and 0.02 g r*GO* were prepared.

Photocatalytic degradation experiments

The conditions and photocatalytic parameters applied in this study are as follows: Since azo dyes are the major contaminants found in the industrial wastewaters, CR was chosen as target pollutant for evaluation of photocatalytic activities.This kind of dye is mainly found in the industrial wastewater and the decomposition of it is difficult. The photocatalytic experiments were performed using 0. 10 g L^{-1} of photocatalyst (MnFe$_2$O$_4$@ZnO-

GO and MnFe$_2$O$_4$@ZnO-rGO and 10 mg L^{-1} of CR solution under natural sunlight irradiation for 35 min. The MnFe$_2$O$_4$@ZnO-rGO and MnFe$_2$O$_4$@ZnO-GO powders were added to10 mg L^{-1} of CR solution in the Pyrex glass beaker containing 50 mL, then they were mixed well under magnetic stirring in darkness for 30 min to obtain adsorption–desorption equilibrium between photocatalyst surface and CR dye molecules. After every 5 min of radiation time, the change in absorbance value of dye was measured by Shimadzu UV-2550PC Model UV-vis spectrophotometer at λ$_{max}$= 500 nm. The photocatalytic activity of the catalysts was calculated regarding of the degradation efficiency (%) of CR by the following equation (1).

$$Degradation = (C_0-C)/C_0*100 \qquad (1)$$

Where C_0 represents the initial CR concentration (mg/L) and C indicates the CR concentration at a certain reaction time (min). The kinetic studies were performed at 25 °C with a concentration range of 0. 10 g L^{-1}, 0.05 g L^{-1} and 0.020 g L^{-1} MnFe$_2$O$_4$@ZnO-rGO and MnFe$_2$O$_4$@ZnO-GO nanocomposites and 10 mg L^{-1} of CR solution with time intervals of (5–35 min) .

RESULTS AND DISCUSSION
Structural study

XRD patterns of the samples were studied in ambient air by using a Philips Xpert XRD. **Fig.1 and Fig.2** demonstrate the X-ray diffraction patterns of synthesized MnFe$_2$O$_4$@ZnO-GO and MnFe$_2$O$_4$@ZnO-rGO and were also compared with the diffraction pattern of GO, rGO and pure MnFe$_2$O$_4$@ZnO in the 2θ ranges from 5 to80°. The average crystallite size for MnFe$_2$O$_4$@ZnO-GO, MnFe$_2$O$_4$@ZnO-rGO and pure MnFe$_2$O$_4$@ZnO from the range of 20-60nm was calculated by using standard Debye-Scherrer equation D=0.9λ/(βcosθ) [26], where D explains the diameter of the nanoparticles, λ (Cu Kα) =1.5406 A° and *β* represents the full-width at half maximum of the diffraction lines. **Fig.1** illustrates the X-ray diffraction pattern of the GO, pure MnFe$_2$O$_4$@ZnO and MnFe$_2$O$_4$@ZnO-GO, respectively. As shown in **Fig.1a**, GO diffraction peaks were observed at 11.89, 26.61, 44.39and 77.24° which corresponds to the (001), (002), (101) and (110) respectively. These diffraction peaks confirmed the hexagonal phase and were directly matched with standard (JCPDS No.00 -041-1487). The X-ray diffraction
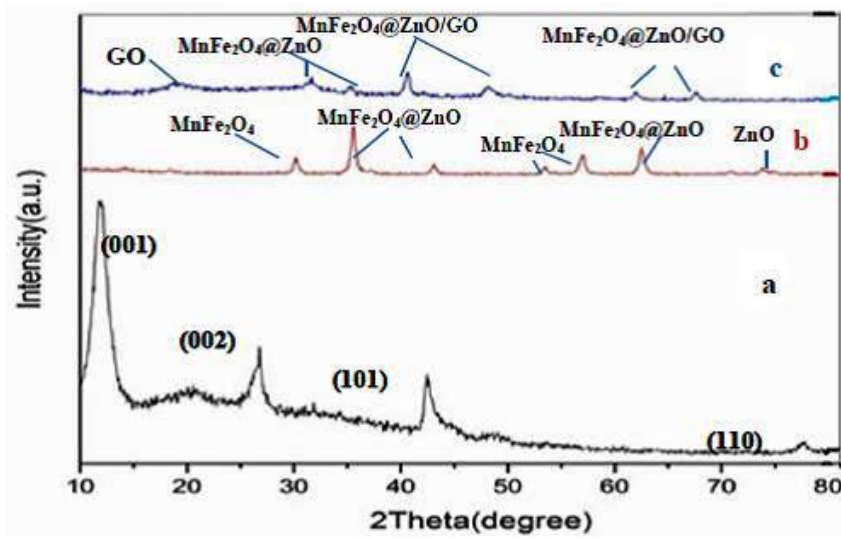
Fig. 1. XRD patterns for (a) GO, (b) MnFe$_2$O$_4$@ZnO and (c) MnFe$_2$O$_4$@ZnO/GO

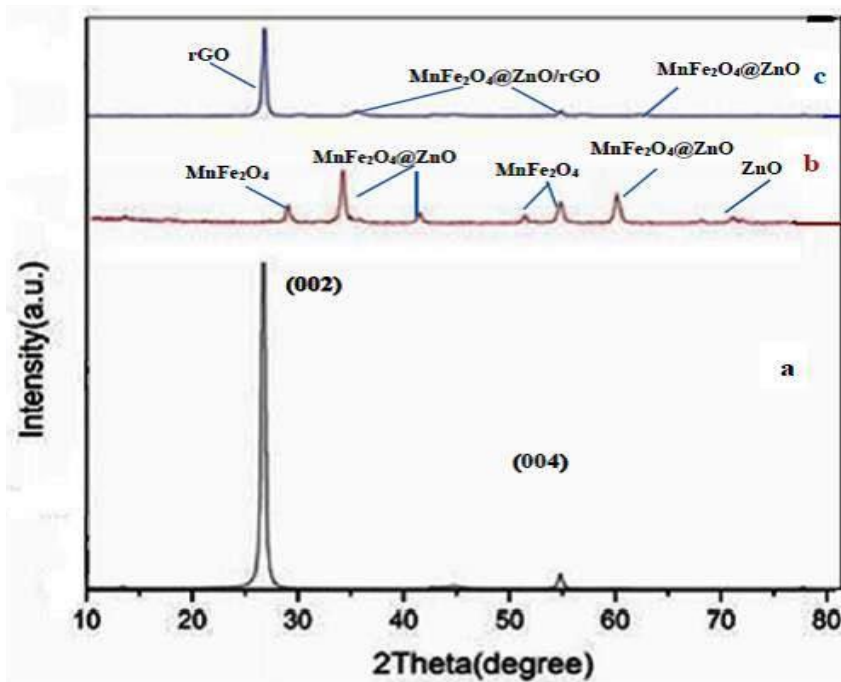
Fig. 2. XRD patterns for (a) rGO, (b) MnFe$_2$O$_4$@ZnO and (c) MnFe$_2$O$_4$@ZnO/rGO

pattern of GO shows a sharp peak centered at 10.89° which corresponds to an interplanar distance of 0.82 nm. An increased interlayer distance between consecutive carbon basal planes is ascribed to the intercalation of oxygen functional groups and water molecules into carbon layer structure. The detectable peak of graphite at 26.61°, corresponding to the highly organized layer structure with an interlayer distance of 0.34 nm along the (002) orientation. Also, two other peaks at 44.39° and 77.24° confirms the crystalline structure of graphite [27]. The X-ray diffraction pattern of MnFe$_2$O$_4$@ZnO was shown in **Fig.1b.** The peaks centered at the angles of 35. 39, 42.93 and 62.30° indicated(113), (004) and (022) respectively, which corresponded to MnFe$_2$O$_4$@

ZnO. Based on the results, The peaks centered at the angles of 18.23, 29.99, 35.33,53.26, 56.77, 70.71 and 74.73 ° indicated (111), (022), (113), (224), (115), (026) and (226) agreed to the cubic phase of $MnFe_2O_4$ which were directly indexed to JCPDS No. 98-006-2998. The peaks centered at the angles of 36.94,42.92,62.31, 74.70and 78.64° indicated (111), (002), (022), (113) and (222) agreed to the cubic phase of ZnO which were directly indexed to JCPDS No. 98-011-6320. **Fig.1c** illustrates the X-ray diffraction pattern of the $MnFe_2O_4$@ZnO-GO. The peaks centered at the angles of 35.45, 53.38, 56.83, 62.46 and 73.90° corresponded to $MnFe_2O_4$@ZnO-GO and also, These diffraction peaks centered at the angles of 30.13° and 43.02° corresponded to $MnFe_2O_4$@ZnO and one diffraction peak was observed at 13.59° which corresponds to graphene oxide. On the other hand, During the hydrothermal process in reaction, crystal growth of $MnFe_2O_4$@ZnO between the interplay of graphene oxide nanosheet mortified the regular layer stacking, which is leading to the exfoliation of GO and the disappearance of the (001) diffraction peak [25]. The X-ray diffraction pattern of the rGO, pure $MnFe_2O_4$@ZnO and $MnFe_2O_4$@ZnO-rGO as portrayed in **Fig.2,** respectively. As shown in **Fig.2a**, rGO diffraction peaks observed at 26.60° and 54.79° corresponded to the (002) and (004) respectively, which demonstrated the hexagonal phase and were significantly resembled with standard (JCPDS No.00 -025-0284). On the other hand, a broad peak shown at $2\theta = 26.60°$, which can be corresponded to an interplanar distance of 0.33 nm along the (002) orientation. This can be explained by the removal of oxygen functional groups, leading to a decrease in d-spacing [28]. The X-ray diffraction   pattern of $MnFe_2O_4$@ZnO was showed in **Fig.2b**. **Fig.2c** displays the X-ray diffraction pattern of the $MnFe_2O_4$@ZnO-rGO. The peaks observed at the angles of 35.52, 42.68, 54.81 and 62.60° corresponded to $MnFe_2O_4$@ZnO-rGO and also, These diffraction peaks centered at the angles of 18.35,30.18,56.85 and 73.97° corresponded to $MnFe_2O_4$@ZnO and one diffraction peak was observed at 26.75° which corresponds to reduced graphene oxide. As portrayed in **Fig. 3(a)** and **Fig. 3(b),** the EDX results showed that C, Zn, Fe, Mn and O elements were clearly present in the $MnFe_2O_4$@ZnO-GO and $MnFe_2O_4$@ZnO-rGO nanocomposites, respectively. The amounts of elements are reported

for the nanocatalyst $MnFe_2O_4$@ZnO-GO   and $MnFe_2O_4$@ZnO-rGO in Tables 1 and2, respectively. The surface morphology of the synthesized materials was analyzed by FESEM as shown in **Fig.4** and **Fig.5**, **Fig. 4a** reveals the formation of a multi-layered of GO nanosheet, while Fig. 4b   indicate the agglomerated spherical shape of $MnFe_2O_4$@ZnO nanoparticles with an average particle size of < 100 nm. Furthermore, It can be shown that the spherical shape of $MnFe_2O_4$@ZnO nanoparticles was unequally decorated on the surface of the GO sheet with an average particle size of < 100 nm in Fig. 4 c, d. Fig. 5 a confirms reduced geraphene oxide wrinkled structure that induced sheet folding [28]. Furthermore, Fig. 5 c, d shows that the surface of the rGO sheet was well decorated with $MnFe_2O_4$@ZnO nanoparticles with the formation of spherical shape and with an average particle size of < 100 nm. Furthermore, the microstructure of $MnFe_2O_4$@ZnO-GO   and $MnFe_2O_4$@ZnO-rGO was examined by using TEM analysis in Figs. 6(a) and6(b), respectively. It can be clearly shown that the microstructure of $MnFe_2O_4$@ZnO-GO   nanocomposites display the   agglomerated   spherical $MnFe_2O_4$@ZnO nanoparticles, which are randomly dispersed over the surface of GO nanosheets as shown in 6(a). Also, Fig. 6(b) indicates the spherical shape microstructure of $MnFe_2O_4$@ZnO-rGO nanomaterials, which are randomly dispersed over the surface of rGO sheets. Additionally, the dark gray nanoparticles ($MnFe_2O_4$) were dispersed on the surface of light gray nano particles (ZnO) as shown in Figs. 6(a) and6(b).

Infrared spectral study

FT-IR analysis was done for a detailed investigation of the obtained samples in the synthesized   GO, $MnFe_2O_4$@ZnO-GO   and $MnFe_2O_4$@ZnO as shown in Fig. **7 (a)**. As shown, the solid state FT-IR spectra of the nanocomposites demonstrated a low intensity bands in the range of 481 and 547 cm^{-1} were assigned to Zn–O and Mn–O stretching vibration band in $MnFe_2O_4$@ZnO, ₍respectively₎. Furthermore, another peak appeared at the 650–500 cm^{-1}which could be attributed to the octahedral group Fe-O. The absorption band around 1644cm^{-1} assigned to stretching vibration of carbonyl group C=O. The stretching vibration of the carboxylate group C=O is shown around 1461 cm^{-1}. Also, The broad peak at 3433.85cm^{-1} is assigned to the stretching and bending modes
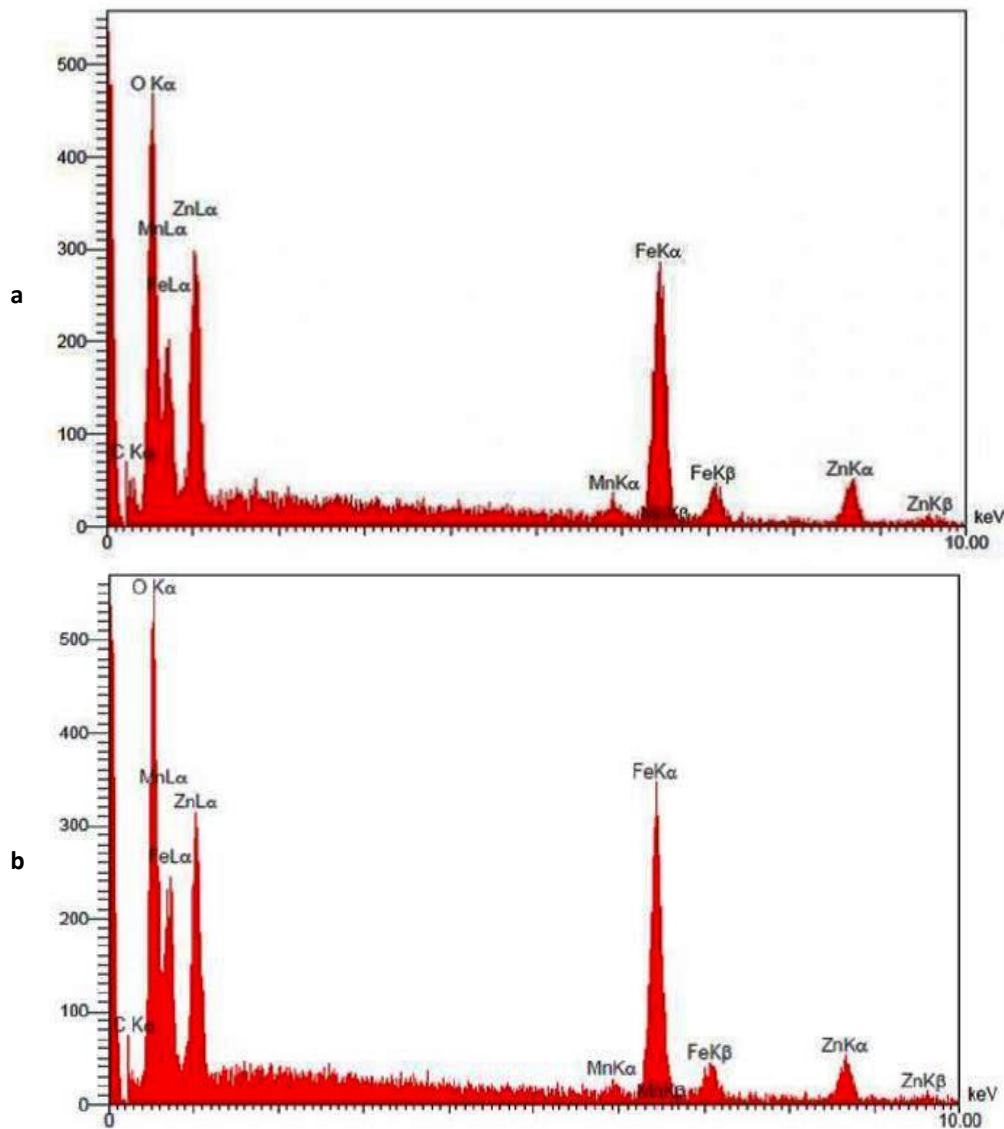
Fig. 3. a) EDAX analyses of MnFe$_2$O$_4$@ZnO-GO nanocomposite b) EDAX analyses of MnFe$_2$O$_4$@ZnO-rGO nanocomposite

Table 1. EDX quantification elements of MnFe$_2$O$_4$@ZnO-GO nanocomposite

Element	C	O	Mn	Fe	Zn	Total
W%	8.84	33.88	1.32	39.39	16.58	100.00
Atom%	19.18	55.20	0.63	18.38	6.61	100.00

of free and absorbed water on the surface of the synthesized MnFe$_2$O$_4$@ZnO nanocomposites [29-30]. The FT-IR spectra confirm the presence of organic impurities in MnFe$_2$O$_4$@ZnO owing to the preparation conditions. For the graphene oxide spectrum, The broad peak was observed at 1038 cm^{-1} in case of GO, which is attributed to the presence of C-O bond, confirming the presence of oxide functional groups after the oxidation process. The peaks in the range of 1625 cm^{-1} to 1650 cm^{-1} exhibit that the C=C bond yet stayed before and after the oxidation process. The peaks were observed around 1200-1380 cm^{-1}, which are related to various C-H stretching vibrations. The
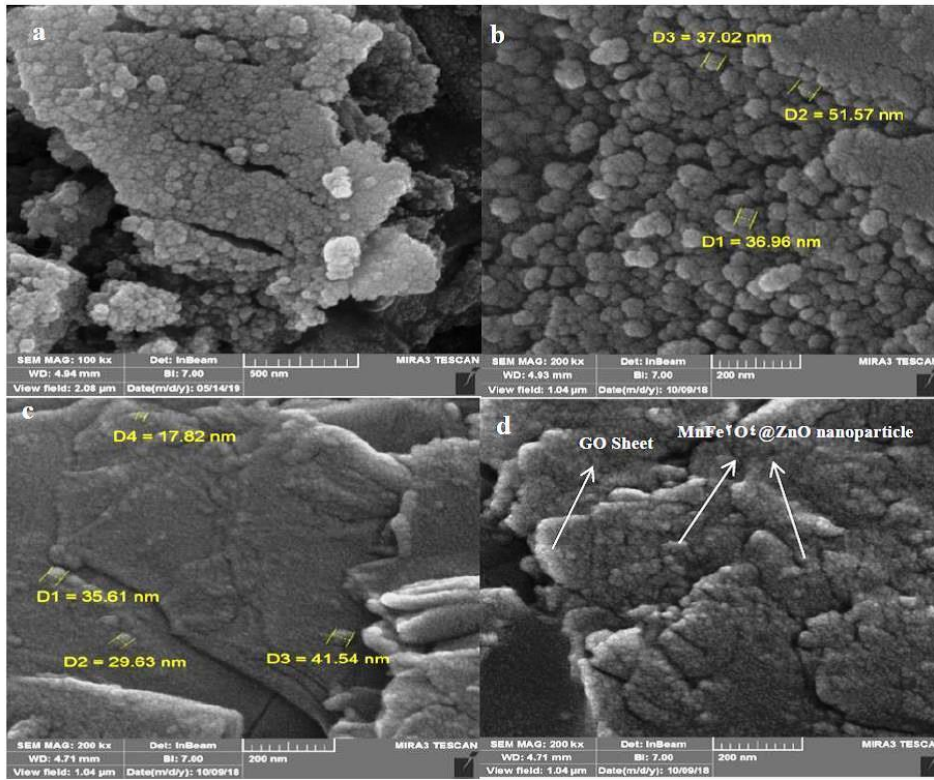
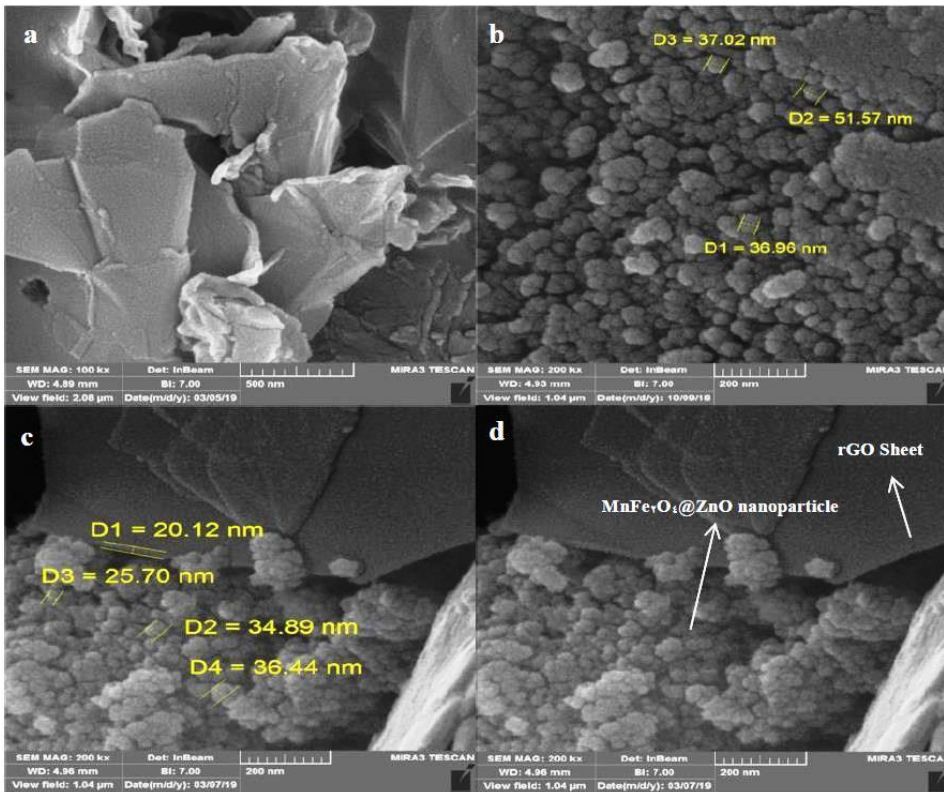Fig. 4. a) FESEM image of GO sheets, b) MnFe$_2$O$_4$@ZnO nanoparticles, c, d) MnFe$_2$O$_4$@ZnO-GO nanocomposites

Fig. 5. a) FESEM image of rGO sheets, b) MnFe$_2$O$_4$@ZnO nanoparticles, c, d) MnFe$_2$O$_4$@ZnO-rGO nanocomposites
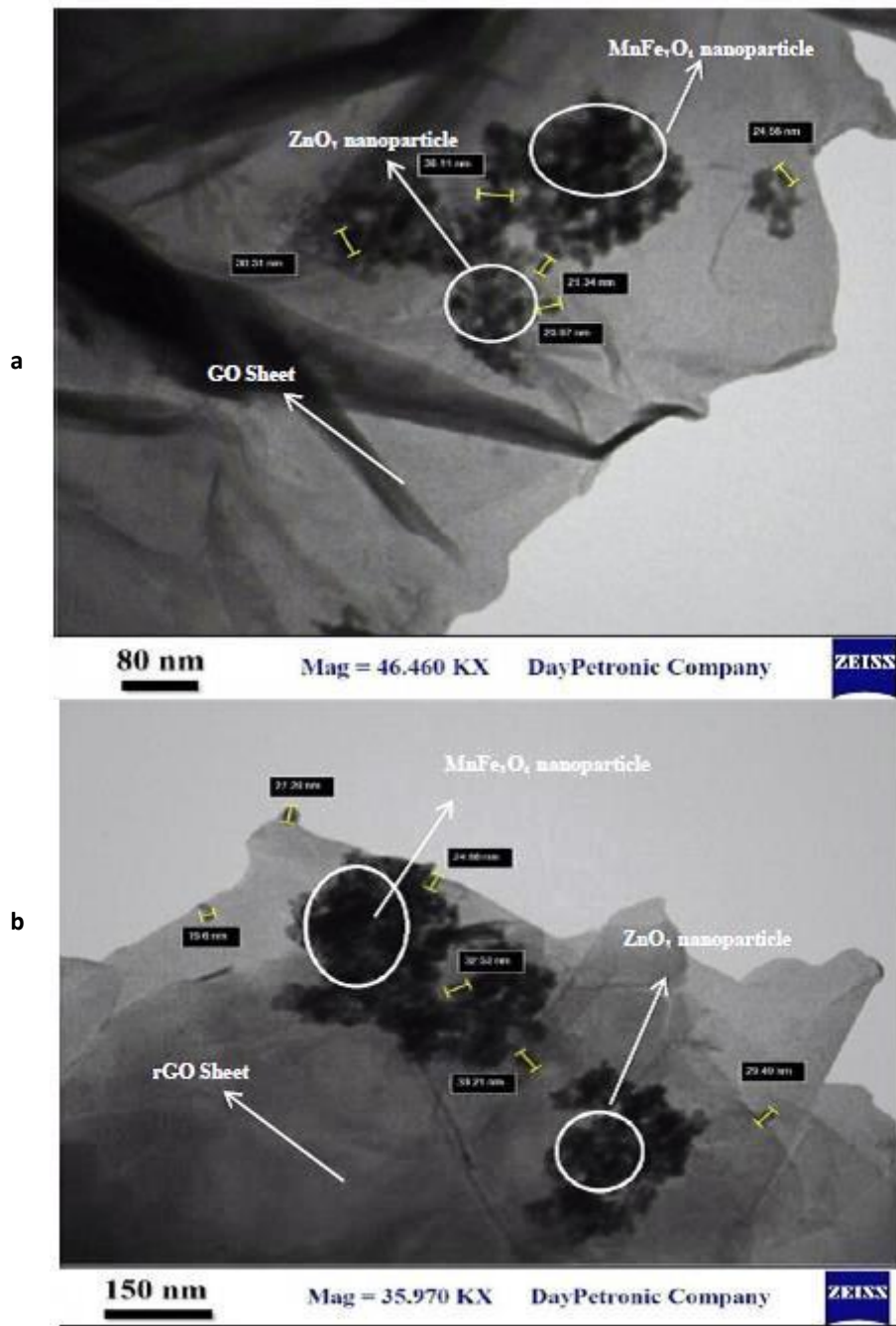
Fig. 6. a)TEM images of the MnFe$_2$O$_4$@ZnO-GO nanocomposites b) TEM images of the MnFe$_2$O$_4$@ZnO-rGO nanocomposites

another peak around 650-850 cm^{-1} is attributed to the presence of C-C out of plane bending. The broad peak at 3417 cm^{-1} to 3715 cm^{-1} is assigned to the O-H stretch of H$_2$O molecules. This confirms the fact that GO is a highly absorptive material, as confirmed by its ability to become a solution similar to gel. The spectrum of MnFe$_2$O$_4$@ZnO-GO nanocomposites shows the distinctive peaks due to MnFe$_2$O$_4$@ZnO and graphene oxide at 430-700 cm^{-1} and 3433.21 cm^{-1}, respectively. And another peaks were observed at 1226 cm^{-1} and 1035cm^{-1}, which are attributed to the presence of the oxygen
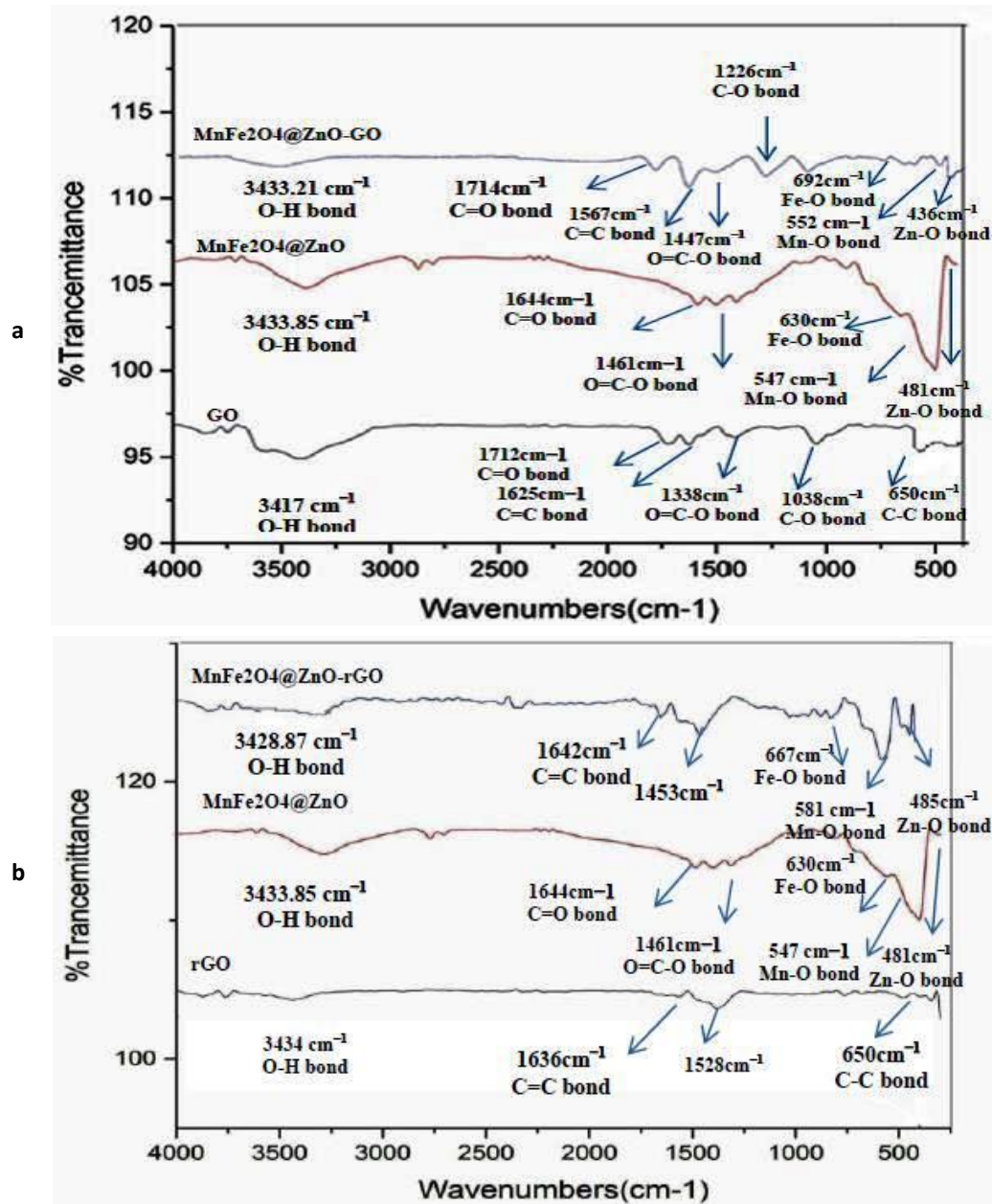
Fig. 7. a) FT-IR spectra of prepared GO, MnFe$_2$O$_4$@ZnO and MnFe$_2$O$_4$@ZnO-GO nanocomposites b) FT-IR spectra of prepared rGO, MnFe$_2$O$_4$@ZnO and MnFe$_2$O$_4$@ZnO-rGO nanocomposites

functional groups on the graphene oxide sheet. Fig. **7 (b)** shows the FT-IR spectra of rGO, MnFe$_2$O$_4$@ ZnO-rGO and MnFe$_2$O$_4$@ZnO nanocomposites. The FT-IR spectrum of rGO displayed no sharp peaks attributing to the oxygen functionalities which confirm the efficient reduction of GO into rGO. Stretching vibrations of O-H groups at 3400 cm^{-1} were missing due to deoxygenation, though

stretching vibration around 2600-2800 cm^{-1} were assigned to the presence of C-H groups, even after the reduction process and stretching vibrations around 1600 cm^{-1}, which can be related to the graphitic domains vertifying the formation of sp^2 carbon structure of rGO. The peak in the range of 1450 -1583 cm^{-1} displays that may be corresponded to the skeletal vibration of the
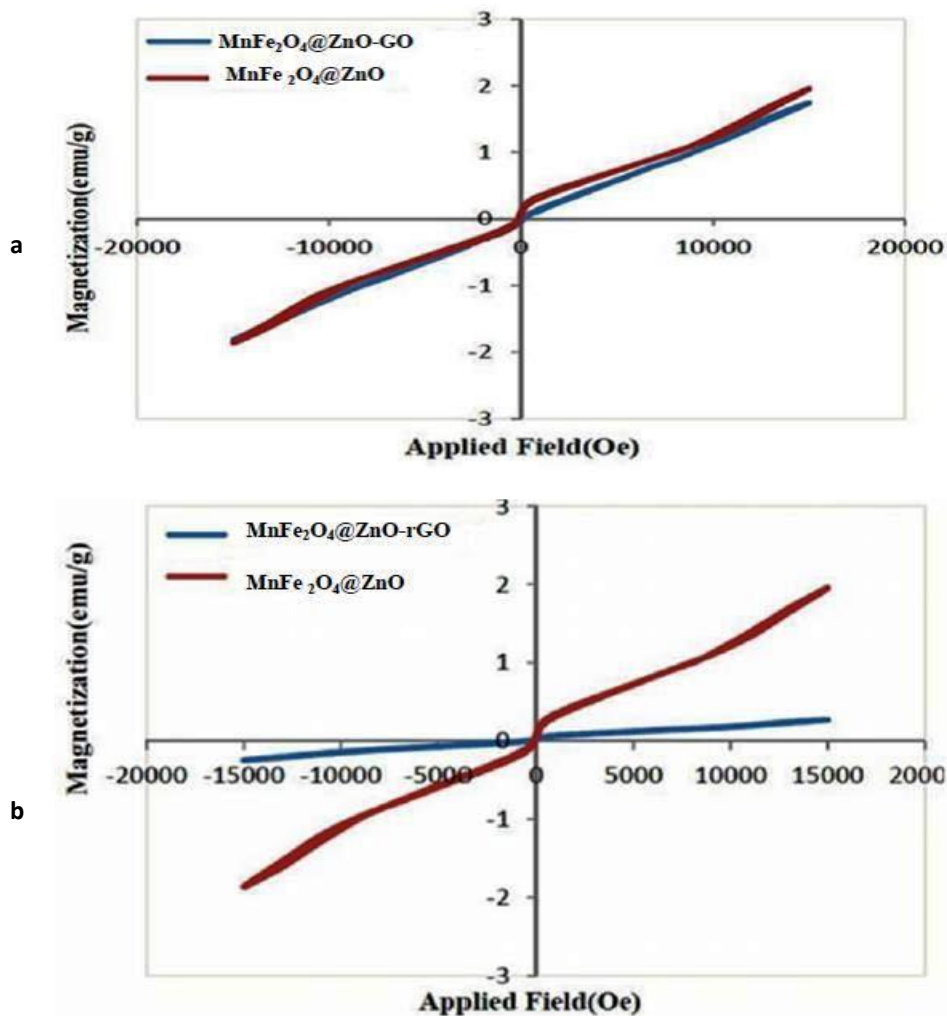
Fig .8. a) Hysteresis curves of MnFe$_2$O$_4$@ZnO and MnFe$_2$O$_4$@ZnO-GO nanocomposites b) Hysteresis curves of MnFe$_2$O$_4$@ZnO and MnFe$_2$O$_4$@ZnO-rGO nanocomposites

reduced graphite oxide [31]. The peak was shown in the ranges 1200-1383 cm^{-1} and 1642 cm^{-1} in case of MnFe$_2$O$_4$@ZnO-rGO, which is attributed to the presence of C-C groups and C=C bond stretching vibrations, respectively. Furthermore, another peak observed in the range 700-500 cm^{-1} and 485 cm^{-1}, which could be attributed to Mn–O stretching vibration band in MnFe$_2$O$_4$, octahedral group Fe-O and   Zn–O stretching vibrations, respectively.

Magnetic properties of MnFe$_2$O$_4$@ZnO-GO and MnFe$_2$O$_4$@ZnO-rGO

The magnetization measurement for the prepared   MnFe$_2$O$_4$@ZnO,   MnFe$_2$O$_4$@ZnO-GO and MnFe$_2$O$_4$@ZnO-rGO nanocomposites was performed using a   vibrating sample magnetometer (VSM) at room temperature. The magnetic hysteresis loops of the synthesized MnFe$_2$O$_4$@ZnO   and   MnFe$_2$O$_4$@ZnO-GO nanocomposites is shown in **Fig .8 (a)**, which indicates that the resulting samples displayed a characteristic of the superparamagnetic behavior with the saturation magnetization of 1.95 and 1.74 emu g^{-1} of MnFe$_2$O$_4$@ZnO and MnFe$_2$O$_4$@ ZnO-GO nanocomposites, respectively. also, the remanent magnetization of MnFe$_2$O$_4$@ZnO and MnFe$_2$O$_4$@ZnO-GO is 0.102 and 0.027 emu g^{-1}, respectively. **Fig. 8 (b)**   explains the hysteresis loops of the MnFe$_2$O$_4$@ZnO and MnFe$_2$O$_4$@ZnO-rGO nanocomposites, The results revealed the superparamagnetic behavior of the synthesized
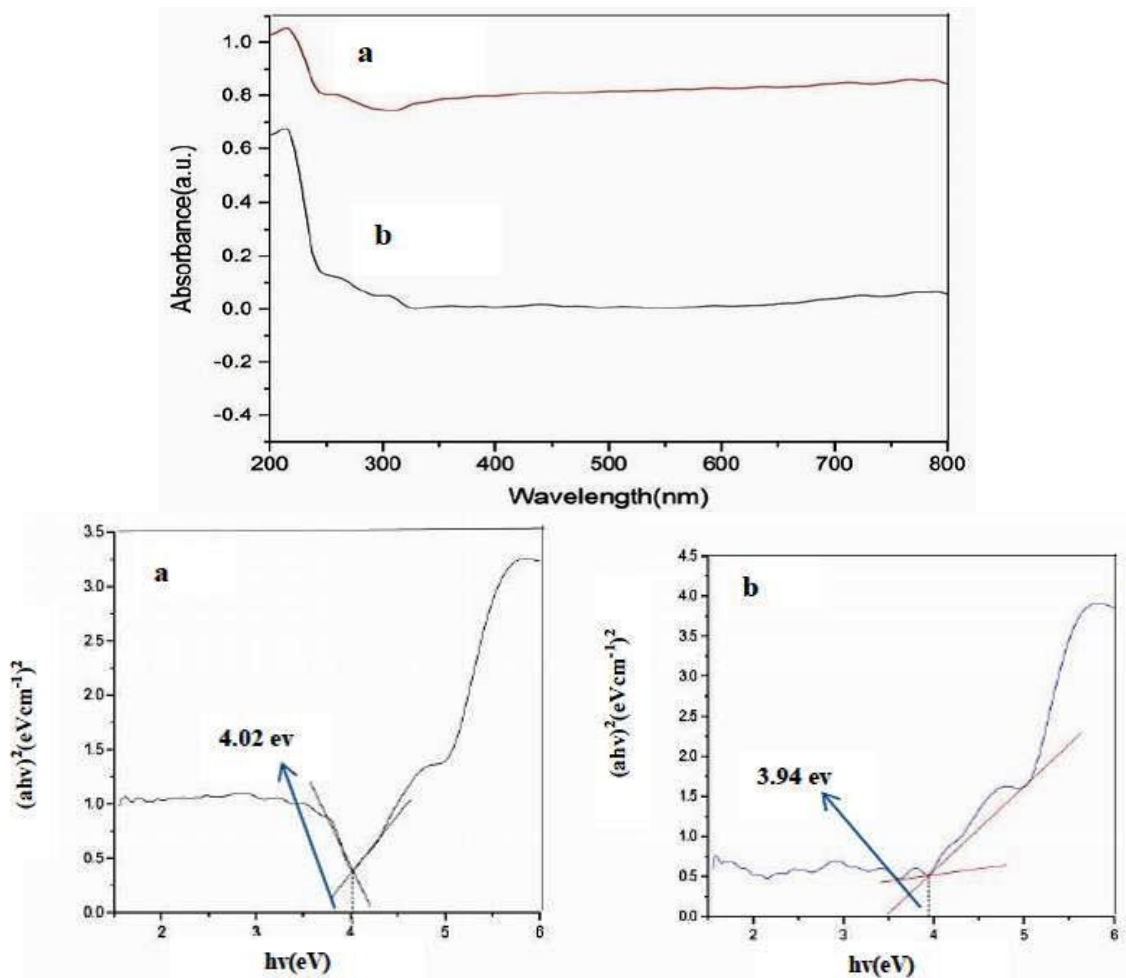
Fig. 9. Optical Absorption Spectrum of a) MnFe$_2$O$_4$@ZnO and b) MnFe$_2$O$_4$@ZnO-GO along with DRS plots of (ahv)^{2}vs. photon energy hv(eV) for c) MnFe$_2$O$_4$@ZnO and d) MnFe$_2$O$_4$@ZnO-GO

samples with the saturation magnetization of 1.95 and 0.27 emu g^{-1} of MnFe$_2$O$_4$@ZnO and MnFe$_2$O$_4$@ZnO-rGO nanocomposites, respectively. Furthermore, the remanent magnetization of MnFe$_2$O$_4$@ZnO and MnFe$_2$O$_4$@ZnO-rGO is 0.102 and 0.032 emu g^{-1}, respectively.   Finally, The results revealed the superparamagnetic behavior of the nanocomposites because of a decrease in the particle size below a critical value (lower than 100 nm). Therefore, the size of the crystalline nature influences the magnetic properties of the nanoparticles [32].

Optical analysis of ZnFe$_2$O$_4$@MnO-GO and ZnFe$_2$O$_4$@MnO-rGO
The optical absorption property related to the electronic structure formation is demonstrated as a key factor in indicating the photocatalytic activity [33]. The optical properties of the prepared MnFe$_2$O$_4$@ZnO, MnFe$_2$O$_4$@ZnO-GO and MnFe$_2$O$_4$@ZnO-rGO samples were carried out by the diffused reflectance UV-vis spectra (DRS), as shown in Figs. 9 and Fig. 10. The UV-Visible absorption spectra of the as-prepared nanoparticles recorded in the range of wavelength 200-800 nm. According to the spectra, all synthesized samples displayed photoabsorption from UV light to visible light region, which shows the possibility of high photocatalytic activity of these nanocomposites under visible light. The band gap of the synthesized materials evaluated from the plot of the transformed Kubelka-Munck function vs. the energy of light [34], is shown in Fig. 6(A) and Fig. 6 (B). The optical band gap energies
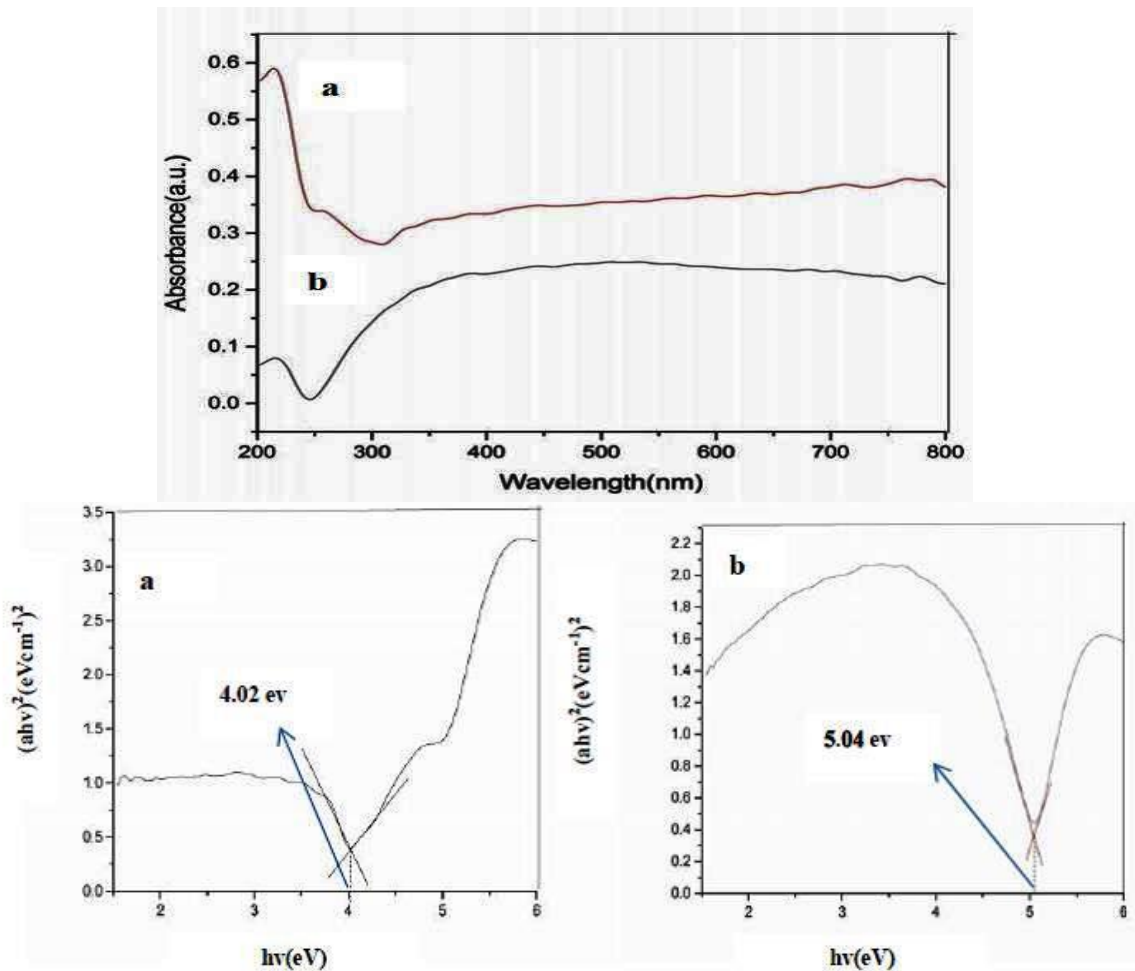
Fig. 10. Optical Absorption Spectrum Of a) $MnFe_2O_4$@ZnO and b) $MnFe_2O_4$@ZnO-rGO along with DRS plots of $(ahv)^2$vs. photon energy hv(eV) for c) $MnFe_2O_4$@ZnO and d) $MnFe_2O_4$@ZnO-rGO

of the synthesized $MnFe_2O_4$@ZnO, $MnFe_2O_4$@ZnO-GO and $MnFe_2O_4$@ZnO-rGO nanocomposites was found to be 4.02, 3.94 eV and 5.04 eV, respectively. The addition of GO lead to the band gap narrowing of $MnFe_2O_4$@ZnO to 3.94 eV for $MnFe_2O_4$@ZnO-GO. Nevertheless, this band gap is yet so large that visible light irradiation ($\lambda > 420$ nm) cannot photoexcite electrons in the valence band (VB) to the conduction band (CB) of $MnFe_2O_4$@ZnO. In relation to structure_photoactivity of $MnFe_2O_4$@ZnO-GO nanocomposite, we suggest a photocatalytic mechanism where the role of GO in the $MnFe_2O_4$@ZnO-GO nanocomposites performs as an "electron transport channel" for $MnFe_2O_4$@ZnO instead of an electron reservoir, hence making they display visible light photoactivity. The results revealed that the addition of GO can narrow the band gap of $MnFe_2O_4$@ZnO (4.02eV) to the

visible light region of ~3.94 ev, which improved the electron–hole separation, leading to enhanced photocatalytic activity. In the case studies, the addition of rGO causes increase the band gap width of $MnFe_2O_4$@ZnO to 5.04 eV for $MnFe_2O_4$@ZnO -rGO. Consequently, this band gap is so large that visible light irradiation ($\lambda > 420$ nm) cannot photoexcite electrons in the valence band (VB) to the conduction band (CB) of $MnFe_2O_4$@ZnO. We propose that in reduced geraphene oxide, a large part of the oxygen functionalities are eradicated, which can be decreased photoexcited electrons transfer from rGO to the CB of $MnFe_2O_4$@ZnO compared to GO in the $MnFe_2O_4$@ZnO-GO nanocomposite. On the other hand, in the $MnFe_2O_4$@ZnO nanocomposite indicates strong bonding interaction among $MnFe_2O_4$@ZnO nanocomposite and GO nanosheets rather than

Table 2. EDX quantification elements of MnFe$_2$O$_4$@ZnO-rGO nanocomposite

Element	C	O	Mn	Fe	Zn	Total
W%	5.72	29.10	2.49	39.16	23.53	100.00
Atom%	13.99	53.47	1. 33	20.62	10.58	100.00

Table 3. BET analysis of GO, rGO, MnFe$_2$O$_4$@ZnO, MnFe$_2$O$_4$@ZnO-GO and MnFe$_2$O$_4$@ZnO-rGO nanocomposites

Samples	Surface area (m^2/g)	Total Pore volum(cm^3/g)	Average pore diameter (nm)
GO[37]	5.86	0.03722	25.37
rGO[37]	11.01	0.05296	19.24
MnFe$_2$O$_4$@ZnO	125.77	0.2218	7.05
MnFe$_2$O$_4$@ZnO-GO	26.34	0.06631	9.18

rGO nanosheets due to the presence of a large number of oxygen-containing the functional group. This is supported by the improved photocatalytic activity of the as-synthesized MnFe$_2$O$_4$@ZnO /GO nanocomposite compared to the MnFe$_2$O$_4$@ZnO / rGO nanocomposite under natural sunlight [35].

Investigation of Porosity and Surface Chemistry (BET)

The nitrogen adsorption–desorption isotherms were used in order to carry out an analysis attribute to the porosity properties MnFe$_2$O$_4$@ZnO-GO and MnFe$_2$O$_4$@ZnO-rGO, and the further interpretation was investigated by using Brunauer–Emmett–Teller (BET) technique. Table 3 represents Total pore volume, average pore diameters and surface area of prepared nanocaomposites, for evaluation of porosity and surface chemistry. The N$_2$ adsorption isotherm and pore size distribution curve of synthesized MnFe$_2$O$_4$@ZnO-GO and MnFe$_2$O$_4$@ZnO-rGO nanocomposites are shown in Fig. 11 (a) and 11 (b). The isotherms demonstrate the features of type IV isotherms with a hysteresis loop at relative high pressures between 0.5 and 0.97 for   MnFe$_2$O$_4$@ZnO-GO nanocomposite, And also, with a hysteresis loop at relative high pressures between 0.4 and 0.98 for MnFe$_2$O$_4$@ZnO-rGO nanocomposite, while the pore size distribution of the BJH is representative of the presence of the mesoporous structures[36]. As given in Table 4, the specific surface area of MnFe$_2$O$_4$@ZnO-GO   and   MnFe$_2$O$_4$@ZnO-rGO nanocomposites are 26.34 m^2/g and19.62 m^2/g with an average pore size diameter of 9.18 nm and 10.57 nm with peaks located at about r$_{p=}$2.4 nm and r$_{p=}$ 2.12 nm, respectively. It is significantly relevant to the mesoporous nature. While the surface area of MnFe$_2$O$_4$@ZnO nanoparticles, GO

and rGO are found to be 125.77 m^2/g, 5.86 m^2/g and 11.01 m^2/g with an average pore size of 7.05 nm, 25.37 nm and 19.24 nm with peaks located at about r$_{p=}$2.4, 3.1, and 1.22 nm, respectively[37]. The lower surface area of MnFe$_2$O$_4$@ZnO-GO and MnFe$_2$O$_4$@ZnO-rGO nanocomposites compared to the MnFe$_2$O$_4$@ZnO can be due to blocking of a few sites by GO and rGO in the MnFe$_2$O$_4$@ZnO structure [22]. Additionally, the surface area of the catalyst is one of the most important factors in photodegradation procedures, higher surface area of the catalyst, causes the generation of more active species and improvement of the photocatalytic activity [38]. The higher the surface area of prepared MnFe$_2$O$_4$@ZnO-GO compared to the MnFe$_2$O$_4$@ZnO-rGO, creates the generation refinement of the photocatalytic performance of the synthesized MnFe$_2$O$_4$@ZnO-GO nanocomposite compared to the MnFe$_2$O$_4$@ZO-rGO nanocomposite under natural sunlight.

Photoluminescence (PL) spectra

Using photoluminescence (PL) spectroscopic analysis, the recombination capability of photo-excited pairs of electron and hole was further was studied [39]. The lower photo-induced recombination of the charge carriers is accepted by the low intensity of PL. Figs. 12 (a) and 12 (b) show the PL spectra of pure MnFe$_2$O$_4$@ZnO, MnFe$_2$O$_4$@ZnO-GO and MnFe$_2$O$_4$@ZnO-rGO nanocomposites. The emission spectra of MnFe$_2$O$_4$@ZnO, MnFe$_2$O$_4$@ZnO-GO and MnFe$_2$O$_4$@ZnO-rGO nanocomposites were recorded in an excitation wavelength of 359 nm at room temperature and the emission spectra emerged at   565 nm, 552 nm and 548 nm, showing a small blue shift, which determines a good interaction between the metal oxide and GO. As this figures represent, the lowest intensity

of PL emission is attributed to MnFe$_2$O$_4$@ZnO-GO sample having a 359 nm excitation wavelength indicating that the photo-generated charge carriers recombination was obstructed in MnFe$_2$O$_4$@ZnO-GO. Thus, compared to pure MnFe$_2$O$_4$@ZnO-rGO and MnFe2O4@ZnO, an increase happened in the time of charge recombination in the MnFe$_2$O$_4$@

ZnO-GO nanocomposite in PL spectra. Resultantly, MnFe$_2$O$_4$@ZnO-GO nanocomposite can significantly increase the photocatalytic behavior because the charge is effectively separated and is efficiently transferred from MnFe$_2$O$_4$@ZnO to the sheets of GO. This proceeding is appropriate for improving the photocatalytic ability compared
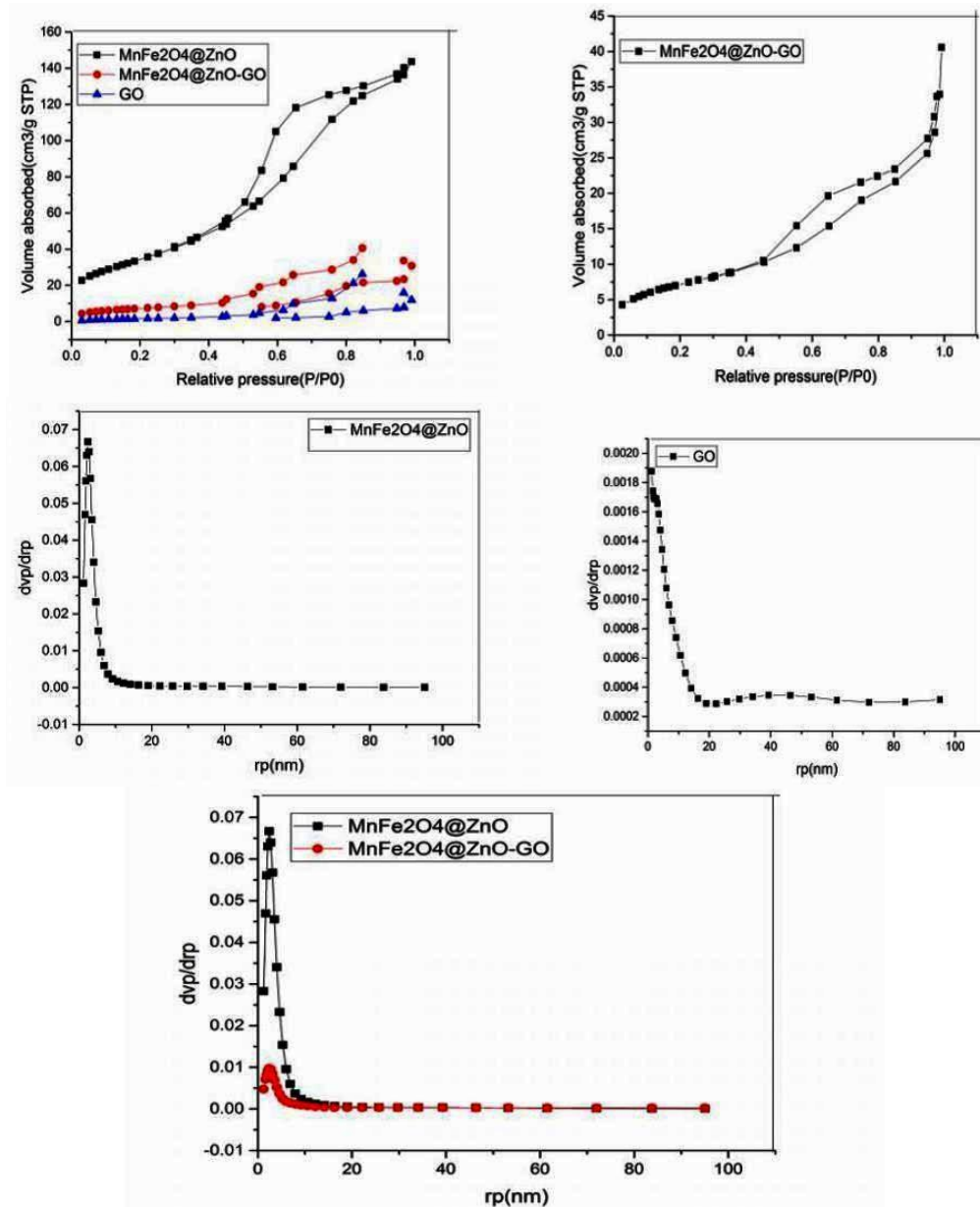

Fig. 11. a) N$_2$ adsorption isotherms of GO, MnFe$_2$O$_4$@ZnO and MnFe$_2$O$_4$@ZnO-GO nanocomposites along with pore size distribution curve
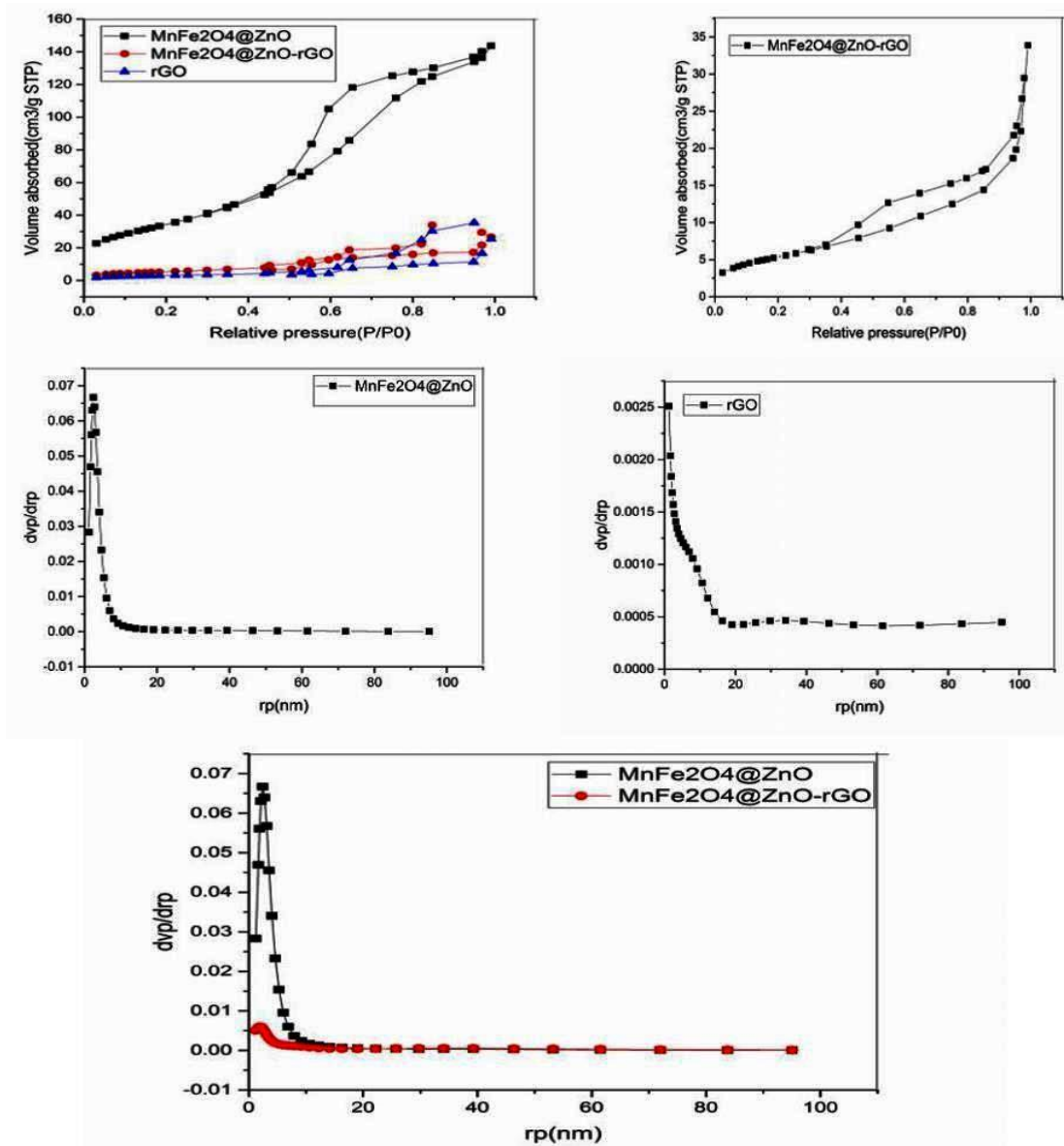
Fig. 11. b) N$_2$ adsorption isotherms of rGO, MnFe$_2$O$_4$@ZnO and MnFe$_2$O$_4$@ZnO-rGO nanocomposites along with pore size distribution curve

Table 4. Rate constant of reaction kinetic for MnFe$_2$O$_4$@ZnO-GO and MnFe$_2$O$_4$@ZnO-rGO photocatalytic degradation by Congo red in different concentrations

Photocata	Initial CR solution concentration, mg/l	Photocatalyst loading, g	k , min^{-1}	R^2
MnFe2O4@ZnO-GO	10	0.10	0.078	0.9957
MnFe2O4@ZnO-GO	10	0.05	0.049	0.9836
MnFe$_2$O$_4$@ZnO-GO	10	0.02	0.045	0.9948
MnFe$_2$O$_4$@ZnO-rGO	10	0.10	0.057	0.9929
MnFe$_2$O$_4$@ZnO-rGO	10	0.05	0.045	0.9839
MnFe$_2$O$_4$@ZnO-rGO	10	0.02	0.042	0.9829
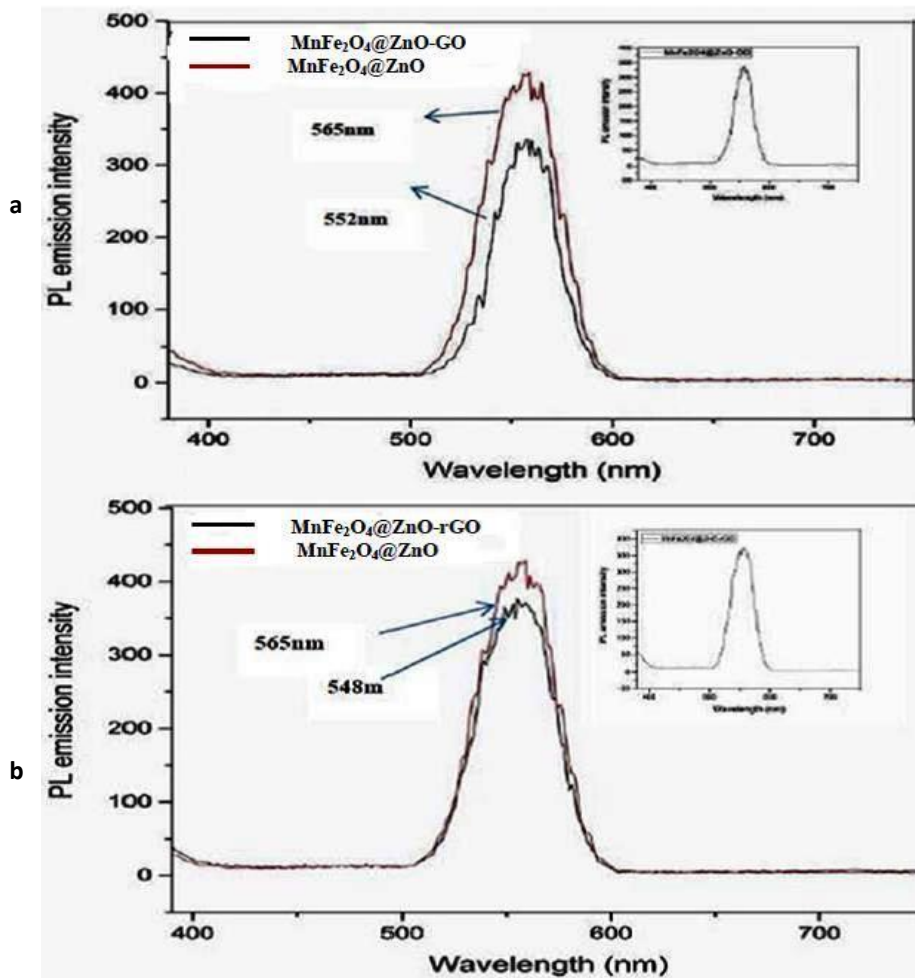
Fig. 12. a) Photoluminescence spectra of MnFe₂O₄@ZnO and MnFe₂O₄@ZnO-GO nanocomposites b) Photoluminescence spectra of MnFe₂O₄@ZnO and MnFe₂O₄@ZnO-rGO nanocomposites

to their bared counterparts (MnFe₂O₄@ZnO and GO). Therefore, the prepared MnFe₂O₄@ZnO-GO nanocomposites might serve as an active photocatalytic factor. Moreover, MnFe₂O₄@ZnO displays strong bonding interaction with GO moiety rather than rGO owing to the presence of a large number of oxygen-containing the functional group. But in reduced geraphene oxide, a large part of the oxygen functionalities are eliminated, which can be made to an unfavorable effect on the photocatalytic capability of MnFe₂O₄@ZnO-GO nanocomposite. This opinion is supported by the improved photocatalytic capability of the synthesized MnFe₂O₄@ZnO-GO nanocomposite compared to MnFe₂O₄@ZnO-rGO nanocomposite under natural sunlight.

Photocatalytic performance of MnFe₂O₄@ZnO-GO and MnFe₂O₄@ZnO-rGO

The photocatalytic efficiency of synthesized MnFe₂O₄@ZnO, MnFe₂O₄@ZnO-GO and MnFe₂O₄@ZnO-rGO nanocomposites was evaluated by using CR dye solutions as a model pollutant under natural sunlight irradiation for time intervals of (5–35 min) at pH=3, as shown in Figs. 13(a), 13(b) and 13(c). In this regard, 100 ml of 10 mg/l CR solution in the presence of 0.10g MnFe2O4@ZnO, MnFe₂O₄@ZnO-GO and MnFe₂O₄@ZnO-rGO nanocomposites were exhibited to the sunlight irradiation. The degradation rate was carried out by decreasing in peak intensity at 498 nm in Figs. 13(a), 13(b) and 13(c). When MnFe2O4@ZnO, MnFe₂O₄@ZnO-GO and MnFe₂O₄@ZnO-
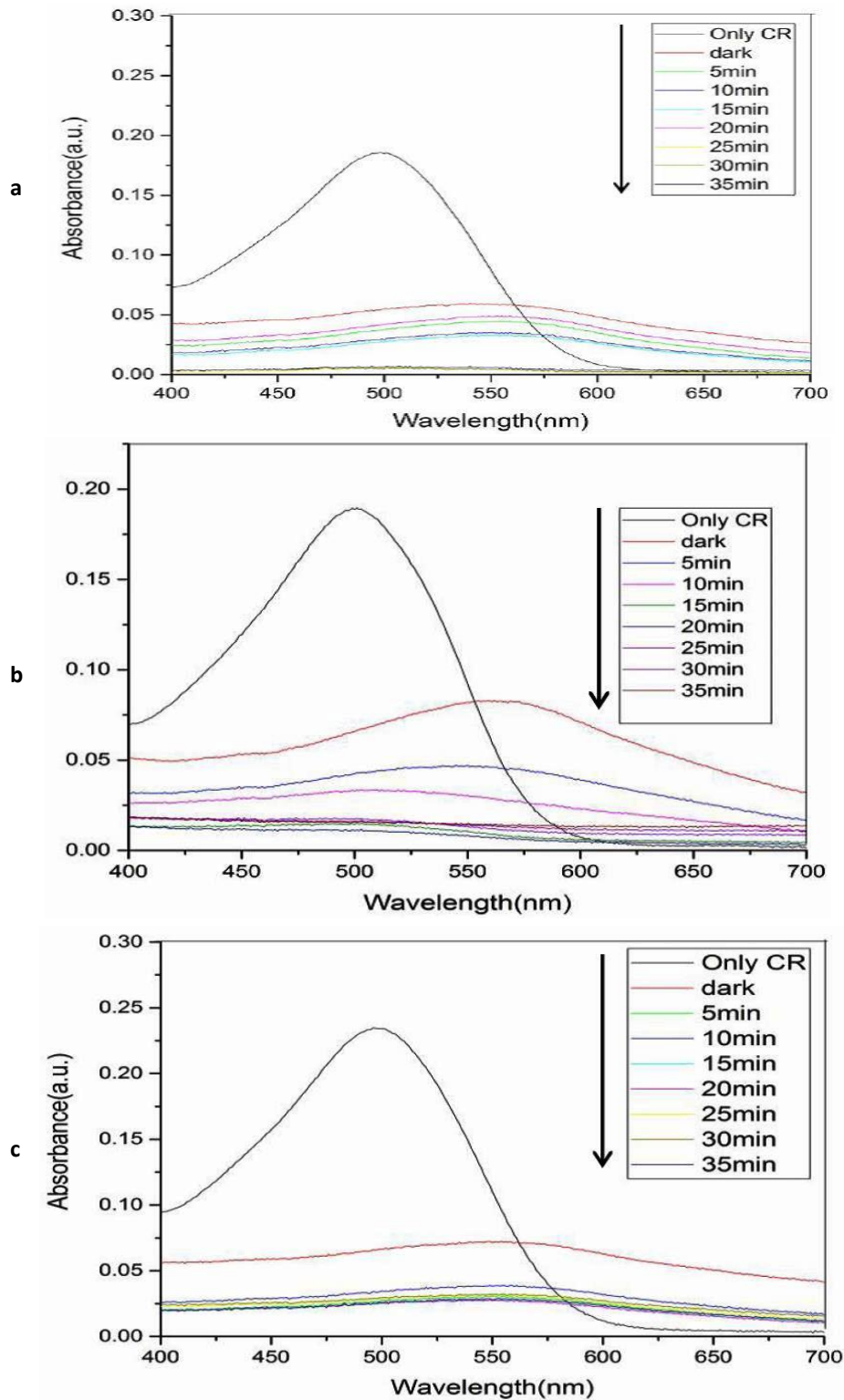
Fig. 13. a) Photocatalytic degradation of Congo red under visible light in presence of MnFe$_2$O$_4$@ZnO b) Photocatalytic degradation of Congo red under visible light in presence of MnFe$_2$O$_4$@ZnO-GO c) Photocatalytic degradation of Congo red under visible light in presence of MnFe$_2$O$_4$@ZnO-rGO

rGO nanocomposites are added into solution and exposed to sunlight for 35 minutes, peak intensity regularly decreases.The results indicated that the percentage of maximum dye degradation in the presence of 0.10g MnFe2O4@ZnO, MnFe$_2$O$_4$@ZnO-GO and MnFe$_2$O$_4$@ZnO-rGO nanocomposites were 92.32 %, 99.54 % and 92.50, respectively. It is clearly observed, that the intensity of absorption peaks decreased for MnFe$_2$O$_4$@ZnO-GO much more than that of MnFe$_2$O$_4$@ZnO and MnFe$_2$O$_4$@ZnO-rGO at 498nm (i.e. wave length of CR absorption) along with the increase in the irradiation time. Degradation efficiency of CR dye by MnFe$_2$O$_4$@ZnO-GO (94.54 % in 35 min) was greater than that of MnFe$_2$O$_4$@ZnO(92.32% in 35 min) and MnFe$_2$O$_4$@ZnO-rGO samples (92.50 % in 35 min). It could be due to the narrower band gap in presence of incorporated GO in the structure of MnFe$_2$O$_4$@ZnO nanocomposite. This phenomenon can be explained that GO acts as a photosensitizer for MnFe$_2$O$_4$@ZnO instead of an electron reservoir in the photocatalytic mechanism in the structure of MnFe$_2$O$_4$@ZnO-GO nanomaterials.

Effects of Initial pH Value

To investigate the effect of pH, several tests were carried out on photocatalyst. The pH of 10mg/l CR dye solution is about 5 in the presence of nanocomposites. Evaluation of the effect of pH was performed in the range of 1-14 by using sodium hydroxide and hydrochloric acid in the dark room. We did not observe the photodegradation of Congo red and we we don't recitation in this research. But when it was irradiated, It was demonstrated that in the pH=1-3, all photocatalysts can only decompose the Congo red, but it does not have the degradation ability in the alkaline pH region 13-14. In the case studies, the least photocatalytic activity was obtained in the pH regions 4-12. Photocatalyst performance of MnFe$_2$O$_4$@ZnO, MnFe$_2$O$_4$@

ZnO-GO and MnFe$_2$O$_4$@ZnO-rGO was carried out at pH= 3 owing to this pH is optimized and nanocomposites gave the best degradation ability in the photocatalytic efficiency of Congo red. The pH factor can significantly affect the ionization degree and CR charge. This phenomenon can be described by the surface properties of the as-synthesized photocatalyst. Congo red is a carcinogenic water-soluble azo dye with two sulfonic groups, as shown in Fig. 14. Two sulfonic acid groups of Congo red can ionize and create a congo red anion. The nanocatalysts MnFe$_2$O$_4$@ZnO-GO in the high acidic regions (pH=1-3) have very higher positive surface potential (Zeta-point charge = +26.5). On the other hand, MnFe$_2$O$_4$@ZnO-rGO nanocatalysts have a positive small surface potential (Zeta-point charge = +12.94) and MnFe$_2$O$_4$@ZnO nanocatalysts have a positive very small surface potential (Zeta-point charge = +9.94) compared with MnFe$_2$O$_4$@ZnO-GO nanocatalyst in the pH=1-3. Therefore, a negative surface charge of CR anion is able to absorb the positive surface of nanocomposite. With an increase in pH value, the Zeta potential reduced by − 19.8 mv in pH 13. Hence, in the acidic region (pH=1-3), photocatalysts are able to degrade the Congo red dye. But in the alkaline region (pH=13-14) photocatalysts only absorb the Congo red. The nanocatalysts in the region between pH=4-12 have a negative surface potential, therefore the interaction and destruction of congo reddye in this area has been minimized. The pH role is better comprehensible when the surface charge of the nanocatalysts is taken into the report. Therefore, in the photocatalytic experiments pH 3 was chosen and nanocomposites gave the best degradation ability in the photocatalytic efficiency.

Effects of dye Concentration

The effect of initial dye (CR), concentration on its photodegradation was performed from
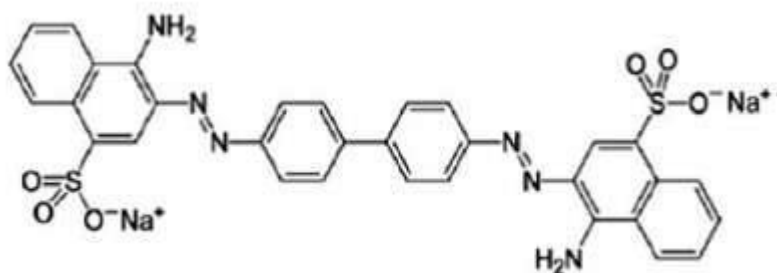

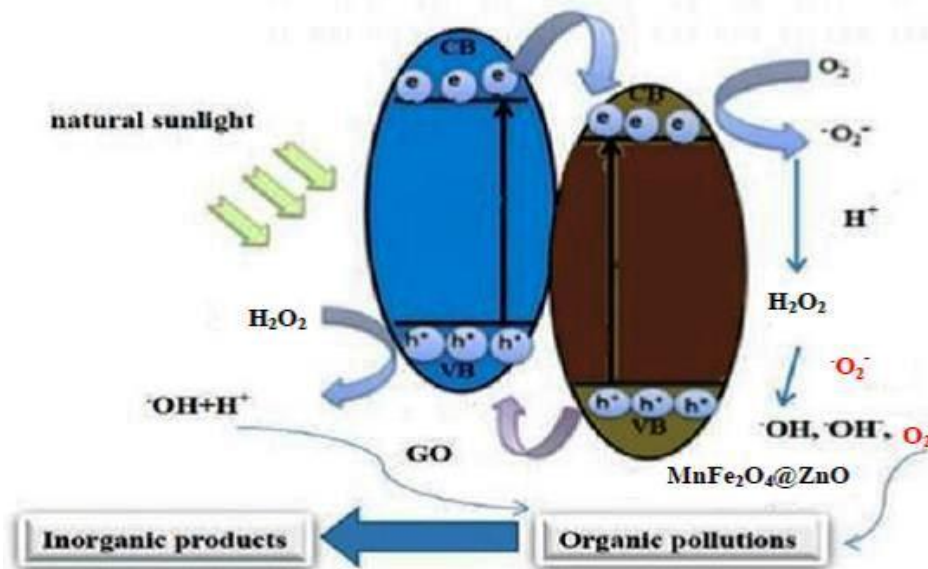Fig.14. congo red structure with two sulfonic groups.

Fig. 15. Mechanism for photodegradation of CR over MnFe2O4@ZnO-GO nanocomposite under natural sunlight irradiation.

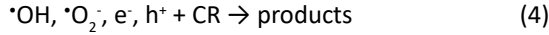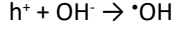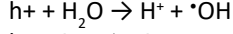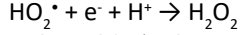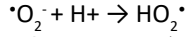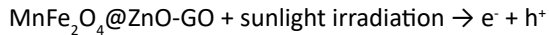10-70 ppm at pH=3and nanocomposites dosage of 0.10g/L in the dark room. We did not observe the photocatalytic activity in the dark and we don't mention in this study. Then, It was exposed to visible light. It is determined that the photodegradation decreases with increase of initial CR concentration. The photocatalysis investigation was carried out in 10mg/l CR solution due to this concentration is optimized and nanocomposites gave the best efficiency in the photocatalytic degradation of Congo red. Resultantly, higher degradation percentage obtained at lower concentrations of dye. At high concentrations due to increased adsorption of dye molecules on photocatalyst surface, active sites are occupied by dye molecules, so the adsorption of O$_2$ and OH$^-$ molecules diminished and then the production of radicals reduced and the degradation rate of the dye reduced [40]. In other words, the formation reactive oxygen species and OH$^-$ molecules on the photocatalyst surface is reduced because the photons are interrupted by the dye molecules before they can reach the catalyst surface. Therefore, At high dye concentrations due to the least photocatalytic activity was found, we don't citation in this research.

Possible photocatalytic mechanism

In photocatalytic degradation carried out in the presence of light, several reactive species

such as photo-generated pairs of electron (e$^-$) and hole (h$^+$), hydroxyl radicals ($^\bullet$OH), superoxide anion radicals ($^\bullet$O$_2^-$) were generated [41]. A photodegradation mechanism is here proposed for degradation of CR applying MnFe$_2$O$_4$@ZnO-GO photocatalyst. This mechanism is displayed in Fig. 15. Electron (e) excitation under irradiation was carried out. The photo-induced electrons moved from the valence band (VB) to the conduction band (CB) of GO. Additionally, in the VB of GO, a similar number of holes (h$^+$) existed. Electrons that were present in the CB of GO were transferable to the CB of MnFe$_2$O$_4$@ZnO since the pairs of electron and hole are obstructed from recombination by the interfacial contact of GO and MnFe$_2$O$_4$@ZnO. As a result, the efficiency of the photocatalytic degradation of the pollution improved. The accumulated surface on the photocatalyst might be trapped by oxygen molecules (O$_2$) for production of the superoxide radical ($^\bullet$O$_2^-$) (Eq. (2)). In this study, CR degradation was induced. As shown in Eq. (3), for the formation of the hydroxyl radical ($\bullet$OH), the photo-induced h+ in VB of GO reacted with the molecules of water or hydroxyl ion (OH), which displayed a synergetic effect of oxidization upon CR. As indicated in Eq. (4), active species like $^\bullet$O$_2^-$, e, h$^+$, and $^\bullet$OH reacted effectively so that CR could be degraded into CO$_2$, H$_2$O or other species. This photocatalytic mechanism for degradation of CR and MnFe$_2$O$_4$@ZnO-GO nanocomposite is

illustrated below.

MnFe$_2$O$_4$@ZnO-GO + sunlight irradiation → e$^-$ + h$^+$

$$O_2 + e^- \rightarrow {}^{\bullet}O_2^- \quad (2)$$

${}^{\bullet}O_2^- + H+ \rightarrow HO_2{}^{\bullet}$

$HO_2{}^{\bullet} + e^- + H^+ \rightarrow H_2O_2$

$$H_2O_2 + {}^{\bullet}O2^- \rightarrow {}^{\bullet}OH + H^+ \quad (3)$$

$h+ + H_2O \rightarrow H^+ + {}^{\bullet}OH$

$h^+ + OH^- \rightarrow {}^{\bullet}OH$

$${}^{\bullet}OH, {}^{\bullet}O_2^-, e^-, h^+ + CR \rightarrow products \quad (4)$$

Kinetics Studies

The Kinetics studies are illustrated by equation lnC$_t$ = lnC$_o$-kt, as shown in Figs. 16(a) and 16(b) . The rate constant value of photodegradation of dye in photocatalytic processes was defined by the pseudo-first-order model which is demonstrated

in the following equation lnC$_t$ = lnC$_o$-kt, where k represents a rate constant (min^{-1}), C$_o$ represents initial absorption, C$_t$ is absorption of CR during reaction process and t is time reaction [42]. The plot of Ln (C$_t$/C$_o$) versus t can be approximated as straight lines, which implies that our approach follows pseudo-first-order kinetics. As a result, Both of the above equations confirmed pseudo-first-order kinetics. Table 4 demonstrates the calculated rate constant and the correlation constants (R^2) under different conditions. The effect of the reaction rate of 0.10 g/L MnFe$_2$O$_4$@ZnO-GO was 0.078 min^{-1}, which was slightly higher, compared to 0.05g/L and 0.02 g/L MnFe$_2$O$_4$@ZnO-GO nanocomposite. Furthermore, The effect of the reaction rate of 0.10 g/L MnFe$_2$O$_4$@ZnO-rGO
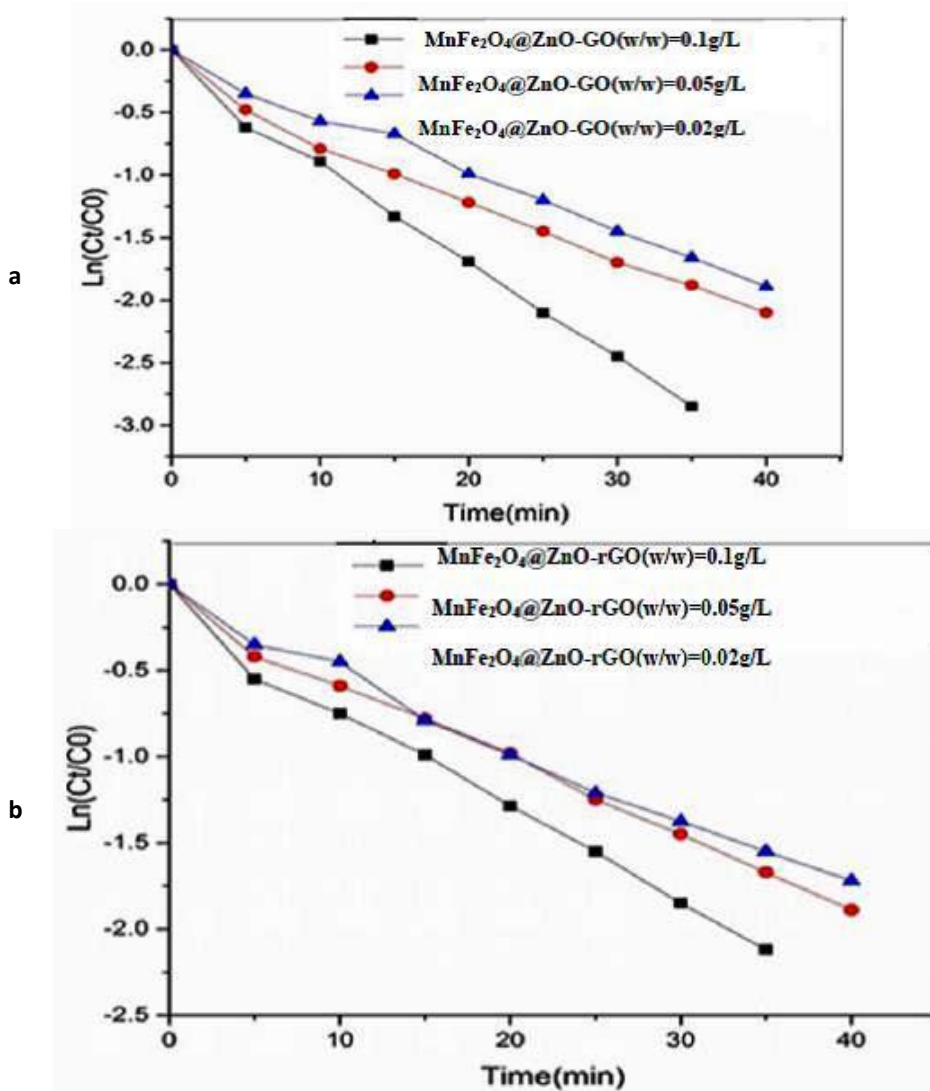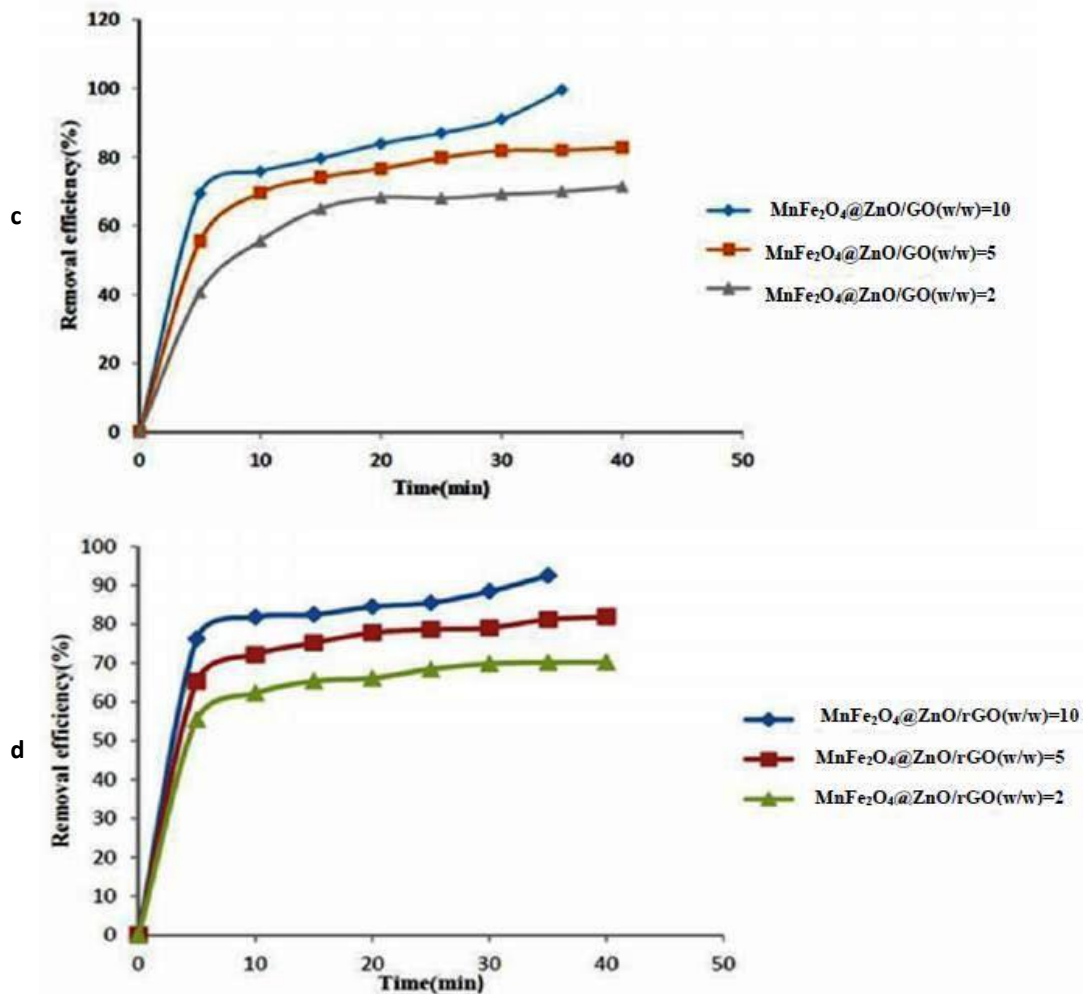
Fig. 16. a) The first order kinetics plot of congo red degradation over MnFe$_2$O$_4$@ZnO-GO b) The first order kinetics plot of congo red degradation over MnFe$_2$O$_4$@ZnO-rGO c) The effect of loading MnFe$_2$O$_4$@ZnO-GO nanocomposite on the CR solutions degradation (Sample: 0.10 g MnFe$_2$O$_4$@ZnO-GO, initial concentration of CR solution: 10 mg/l, pH of CR solution: 4, Volume: 100 ml) d) The effect of loading MnFe$_2$O$_4$@ZnO-rGO nanocomposite on the CR solutions degradation (Sample: 0.10 g MnFe$_2$O$_4$@ZnO-rGO, initial concentration of CR solution: 10 mg/l, pH of CR solution: 4, Volume: 100 ml)

was0.057 min^{-1}, which was some higher, compared to 0.05 g/L and 0.02 g/L the prepared MnFe$_2$O$_4$@ZnO-rGO sample. As a result good photocatalytic activity of MnFe$_2$O$_4$@ZnO-GO under sunlight is related to the high intensity of absorption in the UV–Vis region and band gap energy of as-synthesized composites that is completely in agreement with the results acquired from UV–Vis diffuse reflectance spectra. The photocatalytic degradation of Congo red as a function of time by using the synthesized MnFe$_2$O$_4$@ZnO, MnFe$_2$O$_4$@ZnO-GO and MnFe$_2$O$_4$@ZnO-rGO nanocomposites was investigated under sunlight, as shown in

Fig. 17. It can be explained that the MnFe$_2$O$_4$@ZnO-GO nanocomposites compared to MnFe$_2$O$_4$@ZnO nanocomposites gave the best performance in the photocatalytic degradation of Congo red. Also, It can be demonstrated that the MnFe$_2$O$_4$@ZnO-rGO nanocomposites compared to MnFe$_2$O$_4$@ZnO nanocomposites gave the best efficiency in the photocatalytic degradation of Congo red. The MnFe$_2$O$_4$@ZnO-GO catalyst gave the highest photocatalytic efficiency owing to the well optical absorptions in the UV-Vis region with a lower band gap energy and a larger surface area, which can be contributed to the enhancement in photocatalytic

performance. Further, the graphene oxide in the nanocomposite can act as an electron transfer channel to reduce the recombination of the photo-generated electron holes, leading to improved photo-conversion efficiency [43-44]. Also, in reduced geraphene oxide, a large part of the oxygen functionalities are eliminated, which can be leading to an undesirable effect on the electrical conductivity and other physical properties of it. And its photocatalytic performance has been reduced in the adsorption metal ions, and finally leading to decreasing photocatalytic efficiency.

Effect of catalysts dosage

The amount of photocatalyst is one of the most importantin factors photocatalytic processes, so the value of CR dye removal (10 mg/L) was carried out at different concentrations of photocatalyst (0.1 g/L, 0.05 g/L, 0.02 g/L) in the dark. Therefore, At high concentrations of photocatalyst (0.1 g/L) the least photocatalytic activity was found, we don't mention in this research. So, the value of CR dye removal (10 mg/L) was accomplished at other concentrations of photocatalyst in the dark room. We did not observe the photocatalytic performance in the

dark room. Then, nanocomposites were exhibited to the sunlight irradiation for 35 min. Figures 16(c) and 16(d) displays the influence of catalyst concentration on the photodegradation ability. The photodegradation efficiency of CR is 99.54 % , 82.68%, 71.41%, at 0.1 g/L, 0.05 g/L, 0.02 g/L of MnFe₂O₄@ZnO-GO photocatalyst, respectively. Furthermore, The photodegradation efficiency of CR is 92.50 %, 81.90%, 70.22%, at 0.1 g/L, 0.05 g/L, 0.02 g/L of MnFe₂O₄@ZnO-rGO photocatalyst, respectively. The degradation rate for MnFe₂O₄@ ZnO-GO is much higher than MnFe₂O₄@ZnO-rGO, as shown in Tables 5and 6. This can be concluded that the increment of photocatalytic activity depends on the amount of photocatalyst. The increase in the amount of photocatalyst not only rises the adsorption of dye molecules, but also leads to the improvement in the amount of absorbed photons. Therefore, more active sites are produced at the photocatalyst surface; eventually more free radicals are formed at the photocatalyst surface. As a result, degradation of dye is accomplished with high rate along with the enhanced photocatalyst performance. But when the amount of photocatalyst rises to 16 mg, the dye solution becomes murky and the light cannot
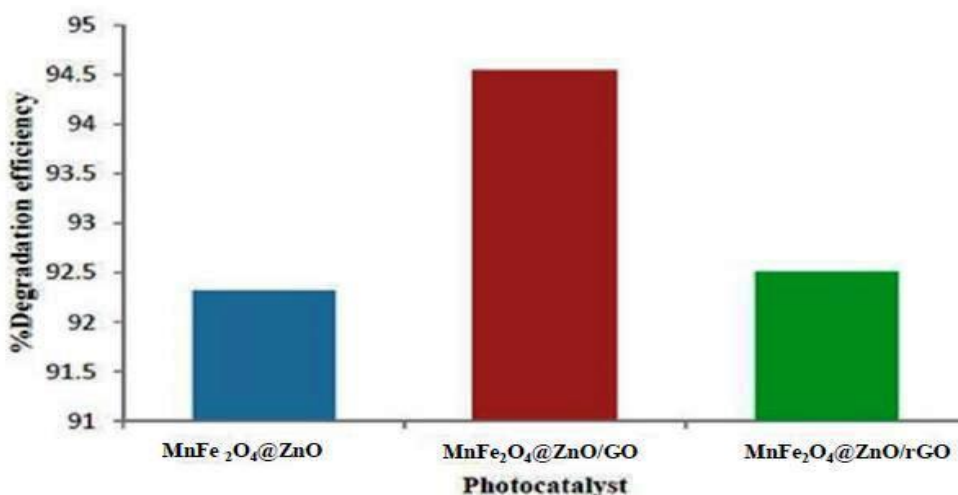
Fig. 17. Comparison of the photodegradation efficiencies of congo red for MnFe₂O₄@ZnO, MnFe₂O₄@Zn-GO and MnFe₂O₄@ZnO-rGO nanocomposites under visible light irradiation for 35 min

Table 5. Compare the degradation rate, (D%) of MnFe₂O₄@ZnO-GO nanocomposite.

Catalysts	D% 5 min	D% 10 min	D% 15 min	D% 20 min	D% 25 min	D% 30min	D% 35 min	D% 40min
MnFe₂O₄ZnO/GO(w/w)=10	69.35	75.8	79.55	83.87	86.94	90.94	99.54	-
MnFe₂O₄ZnO/GO(w/w)=5	55.55	69.55	74	76.6	79.72	81.84	82	82.68
MnFe₂O₄ZnO/GO(w/w)=2	40.61	55.61	64.96	68.23	68	69.1	69.89	71.41

Table 6. Compare the degradation rate, (D%) of MnFe$_2$O$_4$@ZnO-rGO nanocomposite.

Catalysts	D% 5 min	D% 10 min	D% 15 min	D% 20 min	D% 25 min	D% 30min	D% 35 min	D% 40 min
MnFe$_2$O$_4$ZnO/rGO(w/w)=10	76.21	81.79	82.45	84.47	85.47	88.4	92.5	-
MnFe$_2$O$_4$ZnO/rGO(w/w)=5	65.22	72.15	75.21	77.77	78.63	79.05	81.19	81.90
MnFe$_2$O$_4$ZnO/rGO(w/w)=2	55.42	62.22	65.35	66.12	68.42	69.82	70.16	70.22

Table 7. Comparative study of photocatalytic degradation by using optimized concentration of Congo Red dye solution (10 mg/L)

Photocatalyst	Initial CR solution concentration, mg/l	Photocatalyst loading, g	Time(min)	% Degradation
MnFe$_2$O$_4$@ZnO	10	0.10	35	92.32
MnFe$_2$O$_4$@ZnO-GO	10	0.10	35	99.54
MnFe$_2$O$_4$@ZnO-GO	10	0.05	40	82.68
MnFe$_2$O$_4$@ZnO-GO	10	0.02	40	71.41
MnFe$_2$O$_4$@ZnO-rGO	10	0.10	35	92.50
MnFe$_2$O$_4$@ZnO-rGO	10	0.05	40	81.90
MnFe$_2$O$_4$@ZnO-rGO	10	0.02	40	70.22

penetrate well into the solution, as a result, it is not possible to obtain more degradation [45]. On the other hand, the enhanced photocatalytic activity of MnFe$_2$O$_4$@ZnO-GO and MnFe$_2$O$_4$@ZnO-rGO nanocomposites are due to the incorporation of MnFe$_2$O$_4$@ZnO on the GO and rGO sheets which reinforces separation of e⁻/h⁺ pairs and also, When the weight ratio of GO and rGO to MnFe$_2$O$_4$@ZnO rised, the degradation performance increased. This phenomenon is owing to the efficient separation of the electron-hole pairs, which obstructed the recombination rate of e⁻/h⁺ pairs and enhance the photocatalytic degradation rate of pollutants. The comparative photocatalytic investigation of as-synthesized MnFe2O4@ZnO, MnFe$_2$O$_4$@ZnO-GO and MnFe$_2$O$_4$@ZnO-rGO nanocomposites by using CR dye solution under ambient reaction condition was given in Table 7. The optimized concentration of 0.10g synthesized catalysts was elected for further photodegradation studies.

CONCLUSION

In the present study, hydrothermal method was used as a simple and straightforward synthesis method to successfully synthesize MnFe$_2$O$_4$@ZnO-GO and MnFe$_2$O$_4$@ZnO-rGO metal oxide-organic framework nanocomposites with various GO and rGO contents. And also, a facile co-precipitation approach was used for synthesizing MnFe$_2$O$_4$@ZnO nanocomposites with the larger surface area, unique morphology.The photocatalytic performance results indicated that MnFe$_2$O$_4$@ZnO, MnFe$_2$O$_4$@ZnO-GO and MnFe$_2$O$_4$@ZnO-rGO degrade Congo red dye in the same reaction

condition by 92.32 %, 99.54 % and 92.50%, respectively. Our proposed MnFe$_2$O$_4$@ZnO-GO photocatalyst displayed a relatively considerable photocatalytic capability Compared to that of pure MnFe$_2$O$_4$@ZnO and MnFe$_2$O$_4$@ZnO-rGO catalysts to degrade CR as a hazardous pollutant under natural sunlight in 35 minutes. It has been indicated that the visible-light-driven photocatalytic oxidation process for MnFe$_2$O$_4$@ZnO-GO results from a GO photosensitization of MnFe$_2$O$_4$@ZnO, for which upon visible light irradiation no holes are produced due to the wide band gap of MnFe$_2$O$_4$@ZnO not able to be photoexcited by visible light irradiation. The photocatalytic activity results are fitted by performing the calculation of the pseudo-first-order kinetic model. The plot of the Kubelka-Munck function revealed the optical bandgap energy of MnFe$_2$O$_4$@ZnO-GO is relatively less than that of MnFe$_2$O$_4$@ZnO nanoparticle. Compared to pure MnFe$_2$O$_4$@ZnO and MnFe$_2$O$_4$@ZnO-rGO, MnFe$_2$O$_4$@ZnO-GO nanocomposites had much less PL intensity implying a considerable decrease in the photo-induced charge carries recombination. The photocatalytic behavior was improved, since the photo-induced pairs of electron and hole had a low rate of recombination. The combination of the adsorption property of the graphene oxide nanosheet, the magnetic property and GO electron transport property in the MnFe$_2$O$_4$@ZnO-GO nanocomposite compared to MnFe$_2$O$_4$@ZnO-rGO nanocomposite makes the photocatalyst promising candidates for the solution of a variety of environmental problems. We also hope that our work be used for other metal oxide combined

with GO and rGO, and the role of frameworks with different morphologies be considered for controlling other pollutants.

ACKNOWLEDGEMENT

CONFLICT OF INTEREST

The authors declare that there are no conflicts of interest regarding the publication of this manuscript.

REFERENCES

1. Mokhtar Mohamed M, Osman G, Khairou KS. Fabrication of Ag nanoparticles modified TiO 2 –CNT heterostructures for enhanced visible light photocatalytic degradation of organic pollutants and bacteria. Journal of Environmental Chemical Engineering. 2015;3(3):1847-59.

2. Atar N, Olgun A, Wang S, Liu S. Adsorption of Anionic Dyes on Boron Industry Waste in Single and Binary Solutions Using Batch and Fixed-Bed Systems. Journal of Chemical & Engineering Data. 2011;56(3):508-16.

3. Gupta VK, Yola ML, Atar N. A novel molecular imprinted nanosensor based quartz crystal microbalance for determination of kaempferol. Sensors and Actuators B: Chemical. 2014;194:79-85.

4. Alinsafi A, Evenou F, Abdulkarim EM, Pons MN, Zahraa O, Benhammou A, et al. Treatment of textile industry wastewater by supported photocatalysis. Dyes and Pigments. 2007;74(2):439-45.

5. Xu Y, Xu H, Li H, Xia J, Liu C, Liu L. Enhanced photocatalytic activity of new photocatalyst Ag/AgCl/ZnO. Journal of Alloys and Compounds. 2011;509(7):3286-92.

6. Firooz AA, Mahjoub AR, Khodadadi AA, Movahedi M. High photocatalytic activity of Zn2SnO4 among various nanostructures of Zn2xSn1−xO2 prepared by a hydrothermal method. Chemical Engineering Journal. 2010;165(2):735-9.

7. Yassıtepe E, Yatmaz HC, Öztürk C, Öztürk K, Duran C. Photocatalytic efficiency of ZnO plates in degradation of azo dye solutions. Journal of Photochemistry and Photobiology A: Chemistry. 2008;198(1):1-6.

8. Namasivayam C, Arasi DJSE. Removal of congo red from wastewater by adsorption onto waste red mud. Chemosphere. 1997;34(2):401-17.

9. Kamat PV. Photochemistry on nonreactive and reactive (semiconductor) surfaces. Chemical Reviews. 1993;93(1):267-300.

10. Zheng Y, Chen C, Zhan Y, Lin X, Zheng Q, Wei K, et al. Photocatalytic Activity of Ag/ZnO Heterostructure Nanocatalyst: Correlation between Structure and Property. The Journal of Physical Chemistry C. 2008;112(29):10773-7.

11. Chen D, Li Y, Zhang J, Zhou J-z, Guo Y, Liu H. Magnetic Fe3O4/ZnCr-layered double hydroxide composite with enhanced adsorption and photocatalytic activity. Chemical Engineering Journal. 2012;185-186:120-6.

12. Satheesh R, Vignesh K, Suganthi A, Rajarajan M. Visible light responsive photocatalytic applications of transition metal (M=Cu, Ni and Co) doped α-Fe2O3 nanoparticles. Journal of Environmental Chemical Engineering. 2014;2(4):1956-68.

13. Anbarasu M, Anandan M, Chinnasamy E, Gopinath V, Balamurugan K. Synthesis and characterization of polyethylene glycol (PEG) coated Fe3O4 nanoparticles by chemical co-precipitation method for biomedical applications. Spectrochimica Acta Part A: Molecular and Biomolecular Spectroscopy. 2015;135:536-9.

14. Cui L, Guo P, Zhang G, Li Q, Wang R, Zhou M, et al. Facile synthesis of cobalt ferrite submicrospheres with tunable magnetic and electrocatalytic properties. Colloids and Surfaces A: Physicochemical and Engineering Aspects. 2013;423:170-7.

15. Zi Z, Sun Y, Zhu X, Yang Z, Dai J, Song W. Synthesis and magnetic properties of CoFe2O4 ferrite nanoparticles. Journal of Magnetism and Magnetic Materials. 2009;321(9):1251-5.

16. Choi K, Kang T, Oh S-G. Preparation of disk shaped ZnO particles using surfactant and their PL properties. Materials Letters. 2012;75:240-3.

17. Sun L, Li J, Wang C, Li S, Lai Y, Chen H, et al. Ultrasound aided photochemical synthesis of Ag loaded TiO2 nanotube arrays to enhance photocatalytic activity. Journal of Hazardous Materials. 2009;171(1-3):1045-50.

18. Huang H, Li D, Lin Q, Zhang W, Shao Y, Chen Y, et al. Efficient Degradation of Benzene over LaVO4/ TiO2Nanocrystalline Heterojunction Photocatalyst under Visible Light Irradiation. Environmental Science & Technology. 2009;43(11):4164-8.

19. Shi M, Shen J, Ma H, Li Z, Lu X, Li N, et al. Preparation of graphene–TiO2 composite by hydrothermal method from peroxotitanium acid and its photocatalytic properties. Colloids and Surfaces A: Physicochemical and Engineering Aspects. 2012;405:30-7.

20. Feng Q, Li S, Ma W, Fan H-J, Wan X, Lei Y, et al. Synthesis and characterization of Fe3O4/ZnO-GO nanocomposites with improved photocatalytic degradation methyl orange under visible light irradiation. Journal of Alloys and Compounds. 2018;737:197-206.

21. Mzoughi M, W. Anku W, O. B. Oppong S, K. Shukla S, S. Agorku E, P. Govender P. Neodymium Doped ZrO2-graphene Oxide Nanocomposites: A Promising Photocatalyst For Photodegradation Of Eosin Y Dye. Advanced Materials Letters. 2016;7(12):946-50.

22. Das RS, Warkhade SK, Kumar A, Wankhade AV. Graphene oxide-based zirconium oxide nanocomposite for enhanced visible light-driven photocatalytic activity. Research on Chemical Intermediates. 2019;45(4):1689-705.

23. Luo X, Wang C, Wang L, Deng F, Luo S, Tu X, et al. Nanocomposites of graphene oxide-hydrated zirconium oxide for simultaneous removal of As(III) and As(V) from water. Chemical Engineering Journal. 2013;220:98-106.

24. Chen J, Yao B, Li C, Shi G. An improved Hummers method for eco-friendly synthesis of graphene oxide. Carbon. 2013;64:225-9.

25. Gayathri S, Jayabal P, Ramakrishnan V. Hydrothermal synthesis of TiO2-ZnO-graphene nanocomposite towards photocatalytic and photovoltaic applications. AIP Publishing LLC; 2015.

26. Aslibeiki B, Kameli P, Salamati H. The role of Ag on dynamics of superspins in MnFe2−x Ag x O4 nanoparticles. Journal

of Nanoparticle Research. 2013;15(2).

27. Fa J, Hn L, Z Z, Nm H, A P. Titanium dioxide-reduced graphene oxide thin film for photoelectrochemical water splitting. Ceramics International. 2014;40(9):15159-65.

28. Loryuenyong V, Totepvimarn K, Eimburanapravat P, Boonchompoo W, Buasri A. Preparation and Characterization of Reduced Graphene Oxide Sheets via Water-Based Exfoliation and Reduction Methods. Advances in Materials Science and Engineering. 2013;2013:1-5.

29. Vlazan P, Stefanescu M, Barvinschi P, Stoia M. Study on the formation of CoxFe3−xO4 system using two low temperature synthesis methods. Materials Research Bulletin. 2012;47(12):4119-25.

30. Li N, Zheng M, Chang X, Ji G, Lu H, Xue L, et al. Preparation of magnetic CoFe2O4-functionalized graphene sheets via a facile hydrothermal method and their adsorption properties. Journal of Solid State Chemistry. 2011;184(4):953-8.

31. Krishnamoorthy K, Kim G-S, Kim SJ. Graphene nanosheets: Ultrasound assisted synthesis and characterization. Ultrasonics Sonochemistry. 2013;20(2):644-9.

32. Goodarz M, B E. Crystalization in Spinel Ferrite Nanoparticles. Advances in Crystallization Processes: InTech; 2012.

33. Sathishkumar P, Mangalaraja RV, Anandan S, Ashokkumar M. CoFe2O4/TiO2 nanocatalysts for the photocatalytic degradation of Reactive Red 120 in aqueous solutions in the presence and absence of electron acceptors. Chemical Engineering Journal. 2013;220:302-10.

34. Guo H, Chen J, Weng W, Wang Q, Li S. Facile template-free one-pot fabrication of ZnCo2O4 microspheres with enhanced photocatalytic activities under visible-light illumination. Chemical Engineering Journal. 2014;239:192-9.

35. Oppong SOB, Anku WW, Shukla SK, Govender PP. Synthesis and characterisation of neodymium doped-zinc oxide–graphene oxide nanocomposite as a highly efficient photocatalyst for enhanced degradation of indigo carmine in water under simulated solar light. Research on Chemical Intermediates. 2016;43(1):481-501.

36. Wang F, Li F, Zhang L, Zeng H, Sun Y, Zhang S, et al. S-TiO 2 with enhanced visible-light photocatalytic activity derived from TiS 2 in deionized water. Materials Research Bulletin. 2017;87:20-6.

37. Zamani A, Sadjadi MS, Mahjoub A, Yousefi M, Farhadyar N. Synthesis, characterization and investigation of photocatalytic activity of ZnFe2O4@MnO–GO and ZnFe2O4@MnO–rGO nanocomposites for degradation of dye Congo red from wastewater under visible light irradiation. Research on Chemical Intermediates. 2019;46(1):33-61.

38. Karthik R, Kumar JV, Chen S-M, Kumar PS, Selvam V, Muthuraj V. A selective electrochemical sensor for caffeic acid and photocatalyst for metronidazole drug pollutant - A dual role by rod-like SrV2O6. Scientific Reports. 2017;7(1).

39. Huang Y, Gao Y, Zhang Q, Zhang Y, Cao J-j, Ho W, et al. Biocompatible FeOOH-Carbon quantum dots nanocomposites for gaseous NO removal under visible light: Improved charge separation and High selectivity. Journal of Hazardous Materials. 2018;354:54-62.

40. Arunadevi R, Kavitha B, Rajarajan M, Suganthi A, Jeyamurugan A. Investigation of the drastic improvement of photocatalytic degradation of Congo red by monoclinic Cd, Ba-CuO nanoparticles and its antimicrobial activities. Surfaces and Interfaces. 2018;10:32-44.

41. Yu K, Yang S, Liu C, Chen H, Li H, Sun C, et al. Degradation of Organic Dyes via Bismuth Silver Oxide Initiated Direct Oxidation Coupled with Sodium Bismuthate Based Visible Light Photocatalysis. Environmental Science & Technology. 2012;46(13):7318-26.

42. Fayoumi LMA, Ezzedine MA, Akel HH, Jamal MM. Kinetic Study of the Degradation of Crystal Violet by K2S2O8. Comparison with Malachite Green. Portugaliae Electrochimica Acta. 2012;30(2):121-33.

43. Wang D, Li X, Chen J, Tao X. Enhanced photoelectrocatalytic activity of reduced graphene oxide/TiO2 composite films for dye degradation. Chemical Engineering Journal. 2012;198-199:547-54.

44. Ullah K, Zhu L, Meng Z-D, Ye S, Sun Q, Oh W-C. A facile and fast synthesis of novel composite Pt–graphene/TiO2 with enhanced photocatalytic activity under UV/Visible light. Chemical Engineering Journal. 2013;231:76-83.

45. Soltani N, Saion E, Hussein MZ, Erfani M, Abedini A, Bahmanrokh G, et al. Visible Light-Induced Degradation of Methylene Blue in the Presence of Photocatalytic ZnS and CdS Nanoparticles. International Journal of Molecular Sciences. 2012;13(12):12242-58.